Neuron

Article

Intrinsic endothelial remodeling drives brain capillary repair

Graphical abstract

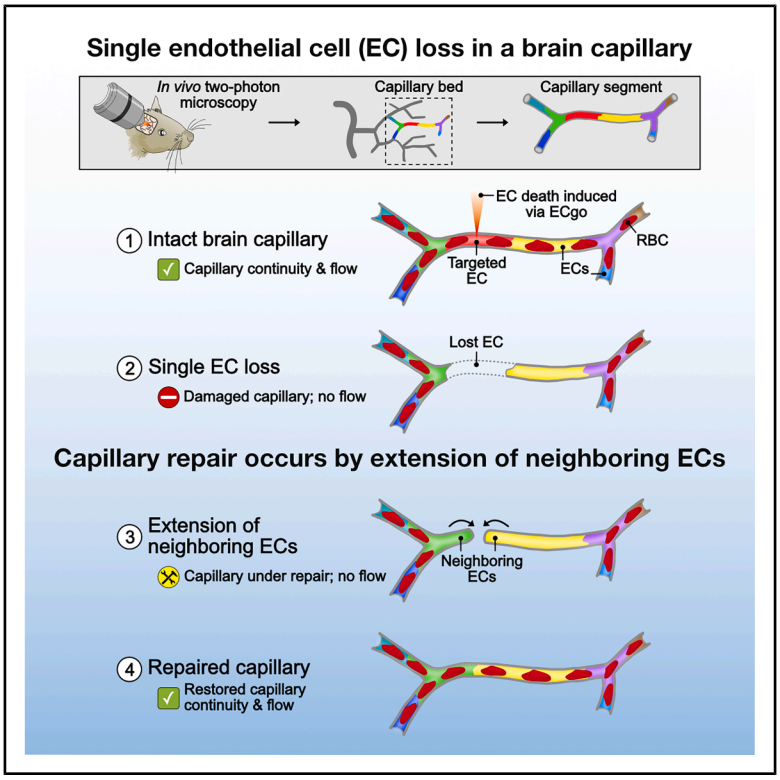

Highlights

- Mouse brain capillaries rapidly repair after local endothelial cell loss
- Neighboring endothelial cells extend to restore capillary continuity and flow
- Capillary repair persists after depletion of microglia, astrocytes, or pericytes
- Hippocampal capillaries show reduced repair compared with cortex

Authors

Jacqueline Condrau, Chaim Glück, Matthias T. Wyss, ..., Sergei A. Vinogradov, Mohamad El Amki, Bruno Weber

Correspondence

bweber@pharma.uzh.ch

In brief

Condrau et al. show that mouse brain capillaries rapidly repair after the loss of a single endothelial cell. Neighboring endothelial cells extend to reconnect the vessel and restore blood flow. Repair persists after depletion of glia and pericytes and differs between cortex and hippocampus, revealing regional variation in vascular resilience.

Condrau et al., 2026, Neuron *114*, 1–15
August 5, 2026
https://doi.org/10.1016/j.neuron.2026.04.020

CellPress

Neuron

CellPress
OPEN ACCESS

Article

Intrinsic endothelial remodeling drives brain capillary repair

Jacqueline Condrau,[1,2] Chaim Glück,[1,2] Matthias T. Wyss,[1,2] Ladina Hösli,[1,2] Eva Erlebach,[1,2] Henri S. Zanker,[1,2] Alexandra von Faber-Castell,[1,2] Luca Ravotto,[1,2] Gina Eberle,[1,2] Srinivasa R. Allu,[4,5] Tatiana V. Esipova,[4,5,7] Thomas Troxler,[4,5] Jeffrey L. Bennett,[6] Marina Herwerth,[1,2,3] Susanne Wegener,[2,3] Aiman S. Saab,[1,2] Sergei A. Vinogradov,[4,5] Mohamad El Amki,[2,3] and Bruno Weber[1,2,8,*]

[1]Institute of Pharmacology and Toxicology, University of Zurich, 8057 Zürich, Switzerland
[2]Neuroscience Center Zurich, University and ETH Zurich, 8057 Zürich, Switzerland
[3]Department of Neurology, University Hospital Zurich, 8091 Zürich, Switzerland
[4]Department of Chemistry, School of Arts and Sciences, University of Pennsylvania, Philadelphia, PA 19104, USA
[5]Department of Biochemistry and Biophysics, Perelman School of Medicine, University of Pennsylvania, Philadelphia, PA 19104, USA
[6]Departments of Neurology and Ophthalmology, Programs in Neuroscience and Immunology, University of Colorado School of Medicine, Aurora, CO 80045, USA
[7]Present address: Department of Chemistry, Loyola University Chicago, Chicago, IL 60660, USA
[8]Lead contact
*Correspondence: bweber@pharma.uzh.ch
https://doi.org/10.1016/j.neuron.2026.04.020

SUMMARY

The brain's microvasculature is essential for oxygen and nutrient delivery; however, the mechanisms underlying cerebral capillary repair following injury remain largely elusive. Here, we identify an unrecognized mechanism through which brain capillary endothelial cells (ECs) autonomously promote capillary remodeling. Using longitudinal two-photon imaging in mice, we demonstrate that following focal endothelial injury and selective loss of a single EC, neighboring ECs extend their plasma membranes toward each other, rapidly re-establishing capillary continuity and blood flow within 24–48 h. This repair process engages vascular endothelial growth factor receptor 2 (VEGFR2) signaling but occurs independently of perivascular or glial cell involvement. Finally, we reveal regional differences in repair efficacy, with hippocampal capillaries exhibiting a slower and less-efficient response compared with those in the cortex. These findings reveal an intrinsic mechanism that safeguards microvascular integrity and suggest that regional vulnerabilities in endothelial repair could shape brain resilience to injury and disease.

INTRODUCTION

The brain is critically dependent on the proper functioning of its intricate vasculature, which ensures a continuous supply of oxygen and nutrients while removing metabolic wastes.[1–4] An elaborate capillary network is formed during development and maintained throughout life to support these functions.[5,6] Endothelial cells (ECs) are critical components of this network, regulating cerebral blood flow and facilitating nutrient-waste exchange.[7] Brain ECs are interconnected through specialized junctional complexes, including tight and adherens junctions, which are essential for establishing the blood-brain barrier (BBB).[8,9] Additionally, ECs interact with pericytes and astrocytes, which contribute to the regulation and maintenance of the BBB, forming an additional layer of structural and functional support.[8–11] Lining the lumen of all blood vessels, brain ECs are continuously challenged by toxic and noxious mechanical stimuli from the blood compartment, triggering EC injury and death, ultimately contributing to vascular failure.[12–14] Given that capillaries typically consist of only 1–2 ECs per segment, the loss of a single EC poses a challenge to brain capillary integrity and function.[15]

Nevertheless, vascular repair mechanisms at the capillary level following EC injury in the brain remain largely understudied. Previous research mainly focused on endothelial repair and recovery in larger vessels,[16,17] showing that endothelial repair can be achieved by either self-replication of resident ECs or by differentiation of EC progenitors, mainly bone marrow-derived, which generate new cells. However, these mechanisms typically occur in large vessels during ischemia or cerebrovascular rupture.[18,19] In contrast, the mechanisms associated with brain capillary repair—particularly after single EC damage—remain poorly understood.

Studies investigating capillary obstructions *in vivo* have primarily focused on intravascular causes of capillary clogging, including individual blood cells[20–24] and microsphere-induced occlusions,[25,26] while relatively little attention has been given to endothelial damage-mediated capillary occlusions and the role

Please cite this article in press as: Condrau et al., Intrinsic endothelial remodeling drives brain capillary repair, Neuron (2026), https://doi.org/10.1016/j.neuron.2026.04.020

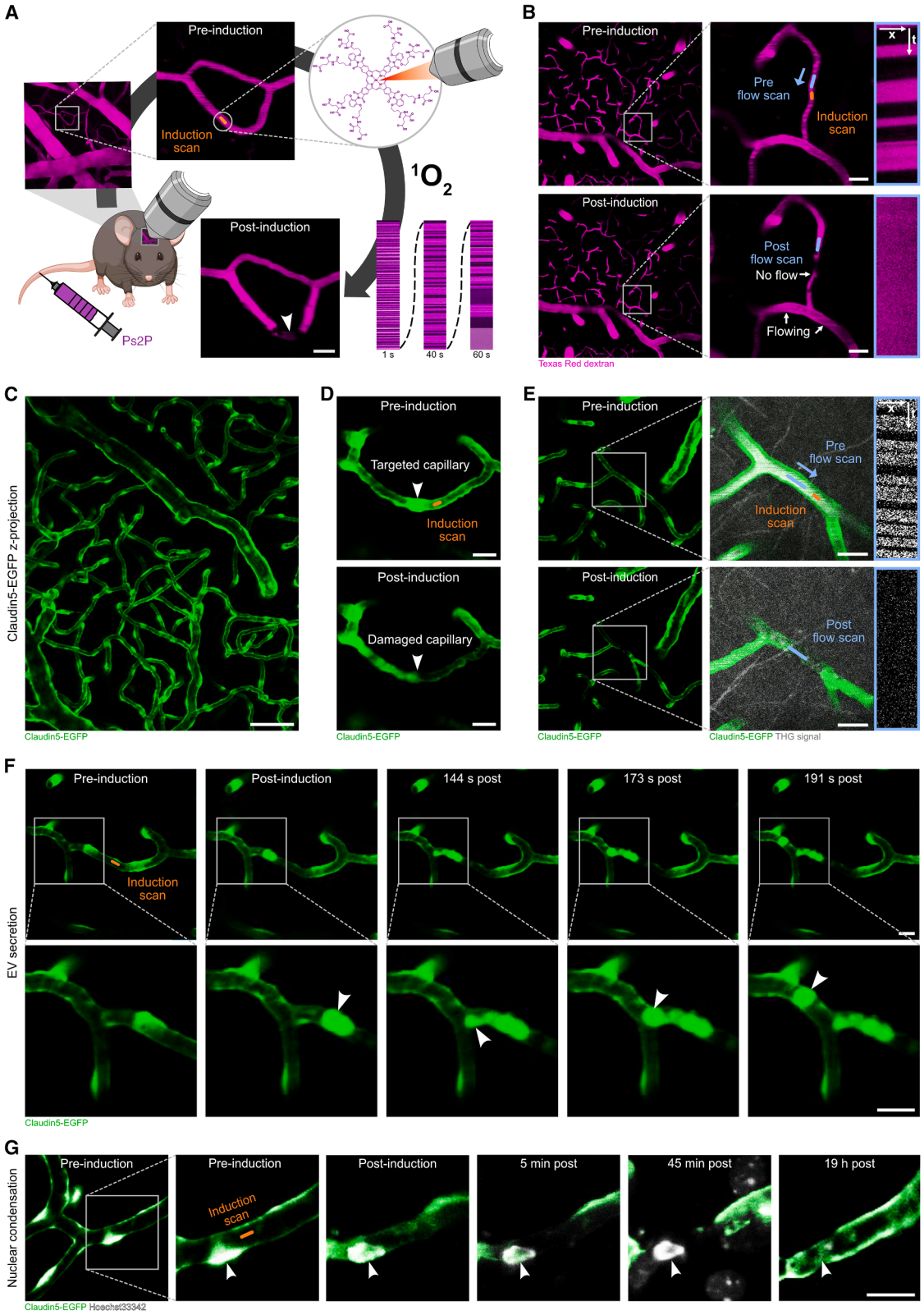

(legend on next page)

of ECs in capillary repair. EC injury and death are closely linked to microvascular pathologies, such as cerebral small vessel disease, and have also been implicated in neurodegenerative diseases, including Alzheimer's disease (AD).[27,28] Hence, understanding EC dysfunction and its role in capillary maintenance and repair is crucial for elucidating their contribution to disease progression.[27,29–31] However, tools to selectively induce targeted and localized EC injury and to investigate its early consequences *in vivo* are still missing. Recently, we introduced ECgo, a new optical method that enables precise occlusion of a single brain capillary via induction of localized EC injury.[32] Here, we utilized ECgo to address several fundamental questions: what are structural and hemodynamic consequences on brain capillary integrity after the loss of a single EC? Are pericytes and glial cells involved in the capillary repair process? Are there regional differences in the capacity for endothelial regeneration?

We found that after single EC injury, brain capillary repair is mediated by the rearrangement of neighboring ECs, which autonomously extend to repair the damaged vessel. This surprising regenerative capacity is vascular endothelial growth factor receptor 2 (VEGFR2)-dependent, highlighting an intrinsic EC feature. Notably, our findings reveal that the hippocampus—a key structure for learning and memory—is less effective at restoring capillary integrity after endothelial damage, suggesting regional differences in capillary remodeling within the brain.

Taken together, this work identifies a previously unrecognized mechanism of brain capillary repair, highlighting the self-sustaining capacity of ECs in maintaining microvascular integrity and underscoring how regional vascular diversity may influence repair efficiency and brain tissue health.

RESULTS

Capillary occlusion by ECgo-mediated single EC ablation

The processes regulating capillary maintenance in the brain are still elusive. We recently developed ECgo, a new approach for localized capillary occlusion in response to a single EC injury.[32] Previous microvascular injury models relied on laser injury or photothrombosis, which severely damaged brain capillaries, causing bursting of vessels and artificially produced clot formation.[33,34] In contrast, ECgo relies on a two-photon-excitable photosensitizer (Ps2P) derived from the Zn complex of tetraarylphthalimidoporphyrin (TAPIP), which binds to plasma albumin and induces local photodynamically driven occlusion of single brain capillaries upon two-photon irradiation (Figure 1A). Immediately after irradiation, blood flow stops in the target capillary segment but not in neighboring capillaries (Figure 1B), confirming that ECgo induces specific and local capillary occlusions as previously demonstrated.[32] Additionally, we previously observed that the underlying reason for capillary occlusion was related to EC injury but not to the formation of an intravascular clot.[32]

We monitored the occluded capillary using time-lapse *in vivo* two-photon imaging to resolve EC behavior following the induced injury. To visualize ECs, we utilized the transgenic mouse line Claudin5-EGFP which expresses EGFP specifically in ECs (Figures 1C and S1A). The nuclear dyes Hoechst33342 or DAPI were used to visualize cell nuclei (Figures 1G and S1A). Notably, following targeted capillary injury, we identified two major hallmarks of EC death: the release of cellular fragments and pyknosis. First, immediately after irradiation, injured ECs released endothelium-derived extracellular vesicles of various sizes (0.7–5.3 μm, Figure S1C) into the downstream vascular segment (Figures 1F and S1D; Video S1). These large vesicles are likely cellular fragments caused by the death of the targeted EC.[35,36] Second, the nucleus of the injured EC underwent pyknosis (chromatin condensation) followed by a single EC death in the targeted capillary (Figures 1G, S1H, and S1I). Consistent with ECgo-induced cell death, the BBB is expected to be transiently perturbed locally, whereas detectable plasma extravasation remained spatially limited and occurred in only ~20% of cases (Figures S1E–S1G). Notably, direct irradiation of the EC nucleus (in the absence of Ps2P injection) failed to induce EC injury or death (Figure S1B). Thus, ECgo is an effective paradigm for single EC ablation *in vivo* without any detectable off-target effects on neighboring ECs or capillaries, making it a useful tool for studying cerebral capillary maintenance and remodeling.

Cortical capillaries repair within 48 h after single EC death

We next sought to investigate the fate of targeted capillaries after single EC loss in the cerebral cortex. We performed longitudinal time-lapse *in vivo* imaging and monitored the targeted capillary segment over 1 week (Figure 2A). Strikingly, the majority of targeted capillary segments regenerated, and blood flow was restored within 24 to 48 h after the induction of single EC death

Figure 1. Optical induction of brain capillary EC injury

(A) Schematic of the experimental workflow. The two-photon-excitable photosensitizer (Ps2P) is administered intravenously and, upon two-photon excitation, induces photodynamically driven capillary occlusion, presumably mediated by singlet oxygen ($^1O_2$). Red blood cell velocity is monitored via line scans. The arrowhead indicates the injured capillary segment. Scale bar: 10 μm.

(B) Representative maximum intensity two-photon 20-μm z projections of capillaries pre- and post-induction with corresponding flow scans on the right side (x, distance; t, time). The blue arrow indicates flow direction. Scale bars: 10 μm.

(C) Representative maximum intensity two-photon 70-μm z projection of brain vasculature from a Claudin5-EGFP mouse. Scale bar: 50 μm.

(D) Single capillary with intact endothelium pre-induction (top) and damaged endothelium post-induction (bottom). Arrowheads pointing to EC nuclei. Scale bars: 10 μm.

(E) Pre- and post-induction two-photon images of a targeted capillary segment. The blue arrow indicates flow direction. Respective flow scans are shown on the right side. THG, third harmonic generation. Scale bars: 10 μm.

(F) Time-lapse images showing EGFP-positive endothelium-derived extracellular vesicles (EVs) released into neighboring vascular segments taken at stated time points. The arrowheads indicate the EV location within the capillary. Scale bars: 10 μm.

(G) EC nuclear condensation indicative of early cell death. The arrowheads are pointing to the EC nucleus. Scale bar: 10 μm.

Please cite this article in press as: Condrau et al., Intrinsic endothelial remodeling drives brain capillary repair, Neuron (2026), https://doi.org/10.1016/j.neuron.2026.04.020

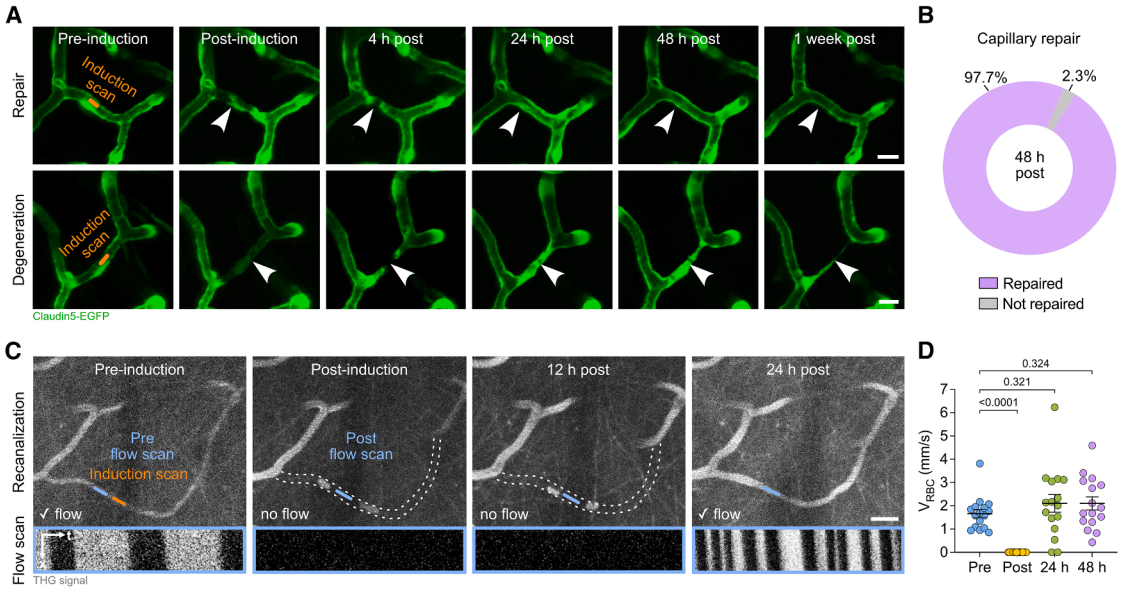

Figure 2. Capillaries exhibit robust repair and recanalization following EC death

(A) Representative maximum intensity two-photon 30-μm z projections of capillary regeneration or degeneration over 1 week post-EC injury. The arrowheads are pointing to targeted capillary segments. Scale bars: 10 μm.

(B) Quantification of capillary regeneration 48 h post-induction (N = 10, n = 43).

(C) Representative maximum intensity 2-photon 20-μm z projections of capillary recanalization over time with corresponding flow scans on the bottom (x, distance; t, time). Dashed lines outline the non-perfused capillary segment post-induction. The capillary is recanalized 24 h post-induction. Scale bar: 10 μm.

(D) Quantification of capillary flow recovery after EC injury (mean ± SEM) within 24–48 h post-induction (N = 5, n = 16).

Data was analyzed by linear mixed-effects model fitted with restricted maximum likelihood, and Tukey-adjusted contrasts for multiple comparisons. N, number of animals; n, number of capillaries.

(Figure 2A, top). Specifically, 97.7% of the targeted capillary segments were repaired and recanalized (i.e., recovery of blood flow) within 48 h (Figure 2B). In rare cases, targeted capillary segments transformed into non-perfused string vessels and degenerated (Figure 2A, bottom). Interestingly, capillary recanalization and blood flow restoration occurred within the same time frame as the structural repair within the first 24–48 h post injury (Figures 2C and 2D). Collectively, these data demonstrate a remarkable microvascular repair capacity in the cortex after single EC loss, highlighting the robustness of the cortex in maintaining its microvascular integrity.

Depletion of microglia, astrocytes, or pericytes does not affect capillary repair

Given that previous work suggests that capillary integrity in the brain is maintained by pericytes[11,37,38] and glial cells, namely microglia[39] and astrocytes,[8,40] we explored the contribution of these cells in capillary repair.

To investigate microglia, we used Cx3cr1-GFP reporter mice (Figure 3A). Following ECgo-induced EC death, we observed fast microglial activation, with processes extending toward the injury site (Figures 3B and 3C; Video S2). Microglial processes rapidly wrapped around the targeted segment, forming a pronounced microglial cast (Figures 3D and S2C, top). These processes began to retract at 8–12 h and were fully retracted by 24 h post-induction, coinciding with capillary recanalization. We did not observe microglial process extension during control irradiation performed in the absence of Ps2P (Figures S2C and S2D, bottom). Next, we tested whether microglia are involved in capillary restoration after EC death. Mice were fed with Plexxikon PLX3397 to deplete microglia.[41] We achieved an approximately 76% depletion of microglia within 1 week of treatment (Figures 3E, 3F, S2A, and S2B). Interestingly, all targeted capillaries recovered in microglia-depleted mice, suggesting that capillary repair after induced EC death is independent of microglia recruitment in our model (Figures 3G–3I).

Next, we asked whether astrocytes could be critical for capillary repair after ECgo-induced EC death. To test this, we depleted astrocytes locally by injecting human-derived aquaporin-4 autoantibodies (AQP4-IgG) into the cortex of Aldh1l1-EGFP mice, as previously described,[42] and targeted selected capillaries 24 h post injection (Figures 4A–4C). Strikingly, despite the clear absence of astrocytes around the targeted vessels, all capillaries were repaired and reperfused within 48 h (Figures 4C and 4D). This suggests that astrocytes are also not essential for capillary repair following EC injury (Figure S2E).

Pericytes interact closely with ECs and were previously described to affect capillary integrity in different vascular injury models.[11,37,43] We therefore asked whether pericytes could contribute to capillary repair after EC death. We used thermal-induced pericyte ablation in the Pdgfrb-tdTomato mice, as previously described[44] (Figures 4E and 4F). We locally ablated 1–3 pericytes 24 h before ECgo induction to allow the capillary segment to recover from the pericyte depletion process.[44]

Please cite this article in press as: Condrau et al., Intrinsic endothelial remodeling drives brain capillary repair, Neuron (2026), https://doi.org/10.1016/j.neuron.2026.04.020

CellPress
OPEN ACCESS

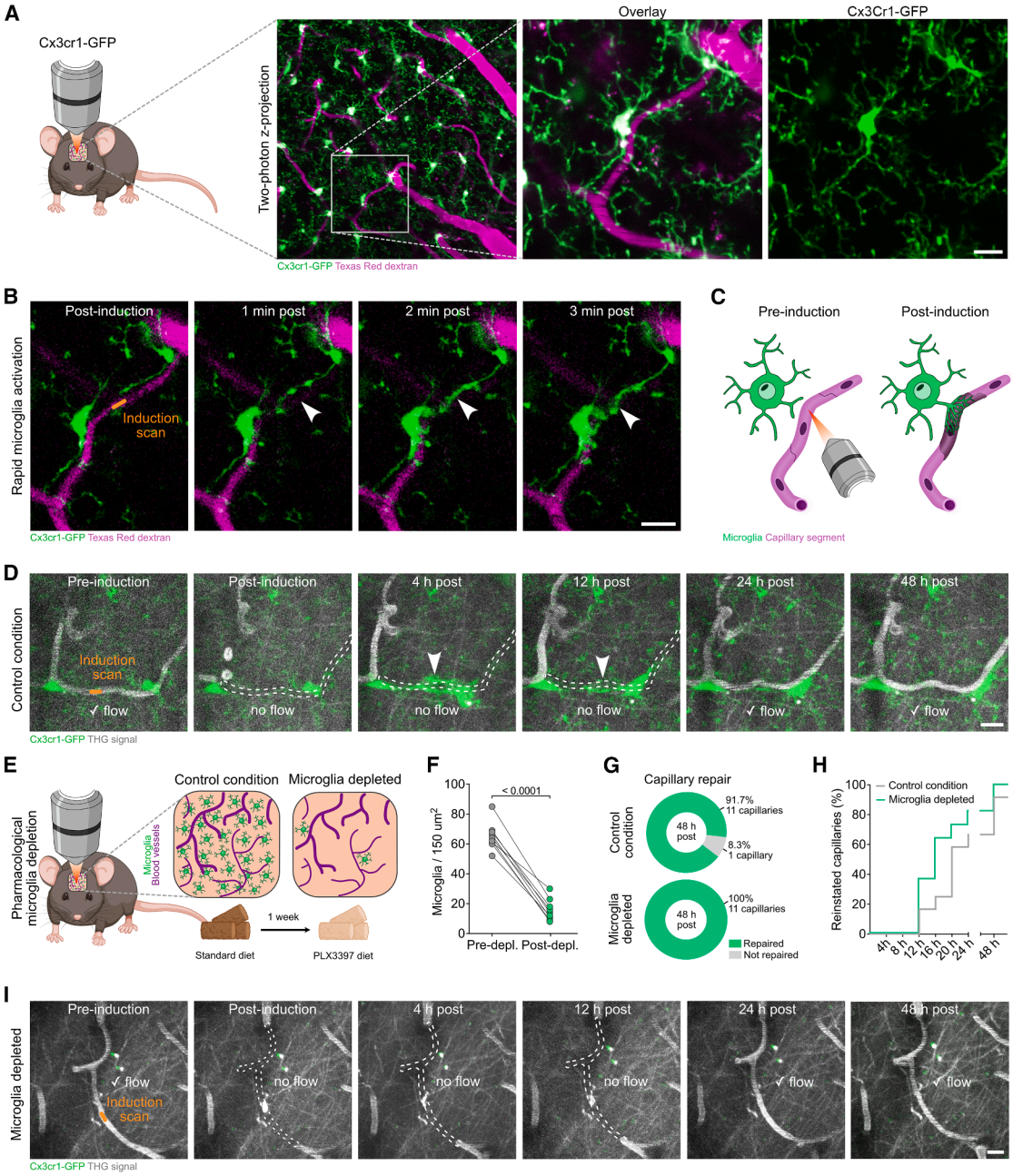

Figure 3. Microglia depletion does not impede capillary recanalization and repair

(A) Maximum intensity two-photon 20-μm z projection of Cx3cr1-GFP mice with fluorescently labeled microglia. Scale bar: 10 μm.

(B) Time-lapse two-photon series showing microglial activation following EC injury induction. The arrowhead indicates microglial processes wrapping around the injured capillary segment. Scale bar: 10 μm.

(C) Schematic of observed microglial activation following EC injury. Microglia extend processes toward the injury site, forming a microglial wrap.

(D) Representative time-lapse maximum intensity two-photon 30-μm z projections of microglial activation upon EC injury induction. The arrowheads mark microglial processes, which retract 12–24 h post-induction. THG, third harmonic generation. Scale bar: 10 μm.

(E) Scheme of PLX3397 microglia depletion protocol.

(F) Quantification of microglia depletion in the cortex (average reduction of 76%); $N = 3$, $n = 9$ regions of interest (ROI) (3 ROI per animal). Data was analyzed by paired t test.

(G) Percentages of recanalized capillaries in control condition ($N = 3$, $n = 12$) and microglia-depleted condition ($N = 3$, $n = 11$) 48 h post-injury induction.

(H) Fraction of reinstated capillaries in baseline condition ($N = 3$, $n = 12$) and post-depletion ($N = 3$, $n = 11$).

(I) Capillary segment over time in a microglia-depleted animal. Maximum intensity two-photon 30-μm z projections. The dashed line marks the previously perfused capillary segment. Scale bar: 10 μm. N, number of animals; n, number of capillaries.

Please cite this article in press as: Condrau et al., Intrinsic endothelial remodeling drives brain capillary repair, Neuron (2026), https://doi.org/10.1016/j.neuron.2026.04.020

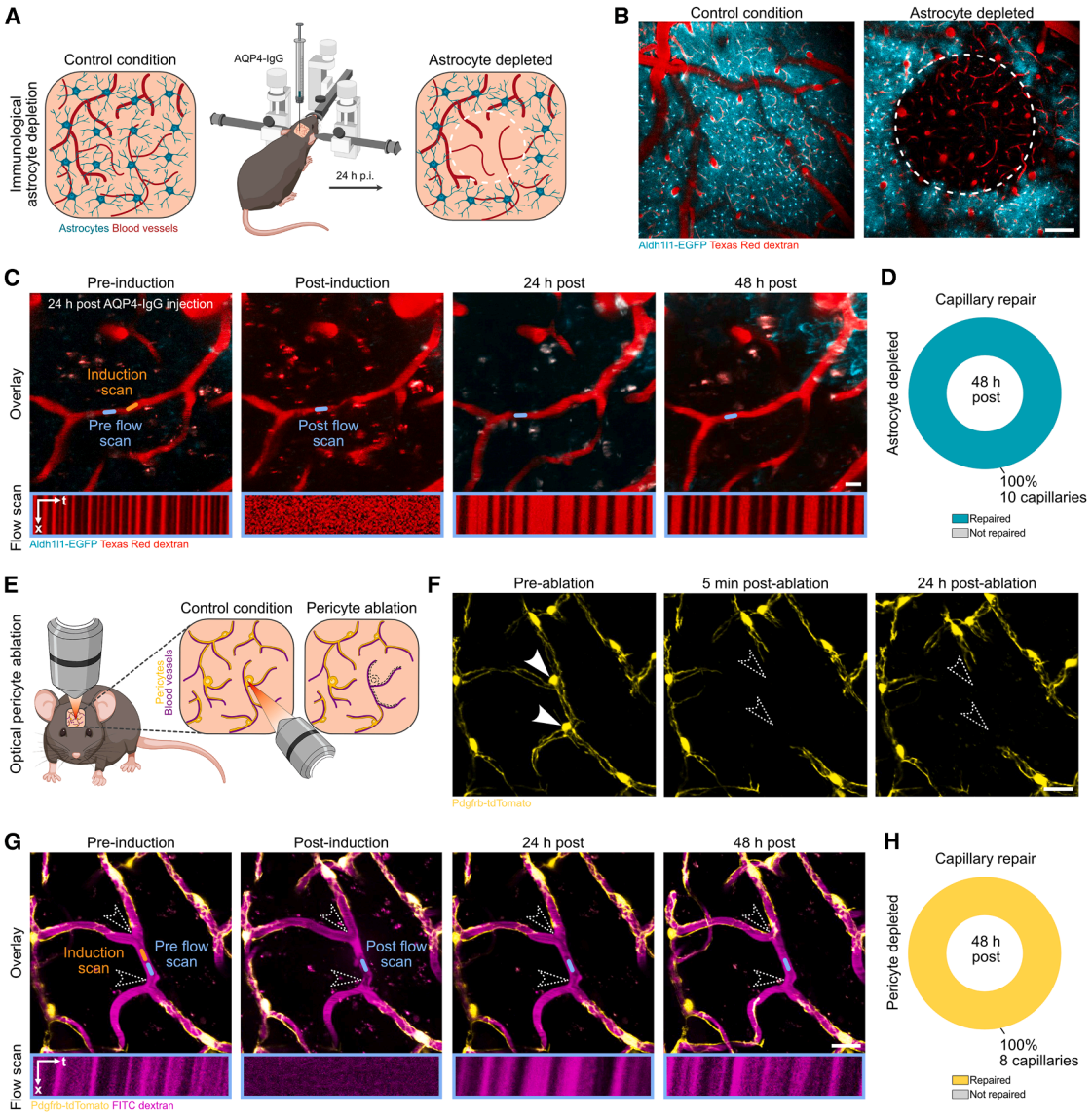

Figure 4. Capillary repair persists following astrocyte depletion or pericyte ablation

(A) Schematic of astrocyte depletion. Intracortical injection of aquaporin-4 autoantibody (AQP4-IgG) in Aldh1l1-EGFP mice induces local astrocyte depletion within 24 h.

(B) Representative two-photon images of control condition and astrocyte-depleted site, outlined by a dashed line. Scale bar: 100 μm.

(C) Exemplary targeted capillary from the astrocyte-depleted region followed over 48 h post-induction. Maximum intensity two-photon 20-μm-z projections. Bottom images show corresponding flow scans (x, distance; t, time). Scale bar: 10 μm.

(D) Recanalized capillaries in astrocyte-ablated condition 48 h post-induction ($N = 2$, $n = 10$).

(E) Workflow of optical pericyte ablation in Pdgfrb-tdTomato mice using a two-photon laser.

(F) Representative maximum intensity two-photon 20-μm z projections of pericyte ablation. Full arrowheads show pericytes pre-ablation; dashed arrowheads indicate post-ablation pericyte absence. Scale bar: 20 μm.

(G) Capillary with ablated pericytes imaged over 48 h. Maximum intensity two-photon 20-μm z projections. Bottom image shows corresponding flow scans (x, distance; t, time). Dashed arrowheads mark ablated pericytes (same as in F). Scale bar: 20 μm.

(H) Recanalized capillaries in pericyte-ablated condition 48 h post-induction ($N = 2$, $n = 8$). *N*, number of animals; *n*, number of capillaries.

Unexpectedly, the absence of pericytes did not affect capillary repair following EC death (Figures 4G, 4H, and S2F). Taken together, neither microglia, astrocytes, nor pericytes appeared essential for capillary restoration, suggesting that the capillary repair mechanism is likely EC-autonomous.

Extension of adjacent ECs drives capillary repair

To determine the role of ECs in capillary repair, we performed longitudinal imaging of individually labeled ECs over the repair period and specifically monitored the fate, density, and dynamics of ECs in the targeted capillary. Given that the process

Please cite this article in press as: Condrau et al., Intrinsic endothelial remodeling drives brain capillary repair, Neuron (2026), https://doi.org/10.1016/j.neuron.2026.04.020

of endothelial regeneration is thought to involve EC proliferation,[16,17,45] we investigated whether a new cell body emerged in the repaired capillary segment. Following capillary repair, the number of EC nuclei was consistently reduced by one, indicating the loss of a single EC and the absence of a newly formed EC in the recovered capillary network (Figures S1H and S1I). Instead, we observed endothelial remodeling during the capillary repair phase, with restoration of the damaged segment progressing from the distal ends of the capillary toward the mid-segment (Figures 2A and S3A).

To gain additional insights into EC remodeling, we used a different EC transgenic reporter mouse line expressing EGFP fused to the tight-junction molecule Claudin5 (EGFP-TJ-Claudin5),[46] which allows the delineating of individual EC boundaries (Figure 5A). Strikingly, we found that following single EC death, neighboring ECs undergo plasmalemmal extension toward the injury site, reinstating the targeted capillary segment within 48 h (Figure 5B). To provide more evidence about how ECs extend their membrane and repair an injured capillary, we sparsely labeled brain ECs using an intravenously injected AAV-BR1-shCAG-tdTomato.[47] This allowed us to visualize the elongation of one labeled neighboring EC after the death of an unlabeled EC (Figure 5C). Notably, our quantifications revealed that neighboring labeled ECs extended, on average, 31.3% of their initial length (Figures 5D and S3B).

To identify the underlying pathway of endothelial-mediated capillary repair, we examined VEGFR2 signaling via the VEGFR2-protein kinase B (Akt)-mTOR pathway (Figures 5E and 5F). Using DC101, a potent VEGFR2 inhibitor,[48] we observed that the fraction of successfully repaired capillaries was reduced at both time points 24 h (68% vs. 100%) and 48 h (84% vs. 100%) post-induction compared with isotype controls (Figure 5F). Given the role of mammalian target of rapamycin (mTOR) signaling in cytoskeletal remodeling and endothelial elongation via mTORC2 signaling,[49] we next evaluated the effect of Ku-0063794, a dual mTOR inhibitor (Figure 5E). Animals treated with Ku-0063794 exhibited markedly reduced capillary repair at 24 and 48 h post-induction (24 h, 50%; 48 h, 60%) relative to controls (24 h, 81.8%; 48 h, 91.9%; Figure 5F).

In the following experiment, we sought to investigate whether EC extension has an upper limit. To address this question, we targeted two adjacent ECs to increase the size of the injured segment (Figure S4A). Indeed, fewer capillary segments were successfully repaired when two adjacent ECs were targeted (Figure S4B). We hypothesize that neighboring ECs extended their membrane but failed to meet each other, leading to capillary regression (Figure S4C).

Hippocampal ECs have a lower capillary repair capacity

Previous studies suggested regional differences in hippocampal and cortical microvascular networks.[50,51] Additionally, the hippocampus is one of the brain regions that is very susceptible to ischemic injury.[52,53] We therefore wondered whether hippocampal capillaries differ in their repair capacities compared with the cortex. To study the hippocampus *in vivo*, we performed a transcortical window surgery, allowing two-photon microscopy imaging of the hippocampal CA1 region[54] (Figures 6A and 6B) and targeting single ECs in hippocampal capillaries (Figures S5A and S5B). Strikingly, we found that capillary repair capacity in the hippocampus was substantially lower compared with the cortex, with only 78.9% of all hippocampal capillaries regenerating within 48 h post-induction (Figure 6B).

To determine whether the diminished EC regenerative capacity in the hippocampus is related to its microvascular architecture, we histologically evaluated both cortical and hippocampal vessel 3D projections (Figure 6C; Videos S3 and S4). We quantified overall vessel densities (encompassing all vessel types) and single capillary segment properties (restricted to capillaries with an abluminal diameter $\leq$ 5.2 μm), including the number of ECs per microvascular segment (Figures 6D and 6E) and its correlation with segment length (Figure 6F). Moreover, we quantified the topological characteristics of the cortical and hippocampal vessel networks, including vessel segment density, single microvascular segment length, microvascular segment straightness, and branch point density (Figures 6G–6N). Consistent with previous findings,[50,51,55,56] we found a reduced vessel volume fraction, vessel length density, and overall segment density in the hippocampus compared with the cortex (Figures S5C–S5G). Despite these differences, the number of ECs per microvascular segment and the average microvascular segment length were comparable between the cortex and hippocampus (Figures 6D–6G). Intriguingly, hippocampal networks contained a significantly greater proportion of straight (i.e., less tortuous) microvascular segments (Figures 6I and 6J). We also observed fewer branch points in the hippocampus, although the number of segments emanating from each branch point was similar in both regions and typically consisted of three connected segments (Figures 6L–6N and S5H).

Thus, although hippocampal capillaries have a sparser and architecturally simpler network, the reduced regenerative capacity of hippocampal capillaries appears to be independent of microvascular segment length or EC distribution, pointing to intrinsic differences in EC-mediated capillary repair between brain regions.

DISCUSSION

We discovered and characterized a yet-unknown mechanism through which brain ECs autonomously drive capillary repair after injury. Notably, this process proceeds independently of critical support from microglia, pericytes, or astrocytes. In addition, we revealed that cortical capillaries exhibit a higher regenerative capacity than hippocampal capillaries, suggesting distinct regional differences in capillary repair. These findings augment our mechanistic understanding by which the brain maintains capillary integrity when an EC dies due to microvascular injury.

Despite being continuously exposed to potentially noxious stimuli such as blood-derived pathogens or biomechanical stimuli, ECs effectively maintain vascular integrity throughout life.[57] Until now, models to specifically study microvascular dysfunction due to localized EC death have been lacking. Previous studies locally disrupted brain capillary integrity using optical methods such as ultrashort repetitive laser pulses[33] or the activation of the photosensitizer Rose Bengal for targeted capillary photothrombosis.[58–60] However, these approaches either induced large vascular ruptures or clot formation, limiting the

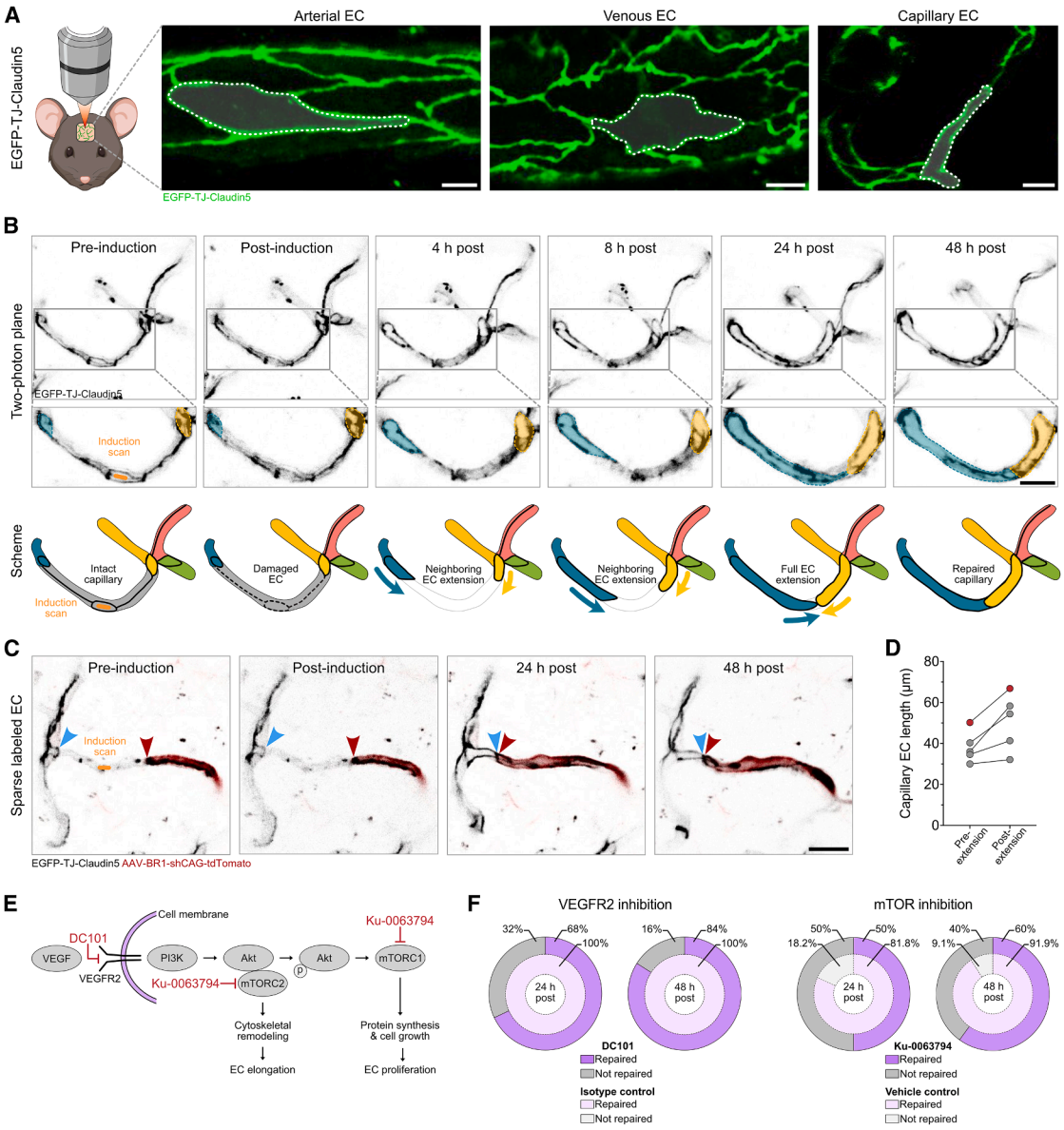

Figure 5. Capillary repair is facilitated by neighboring EC extension

(A) Representative two-photon images from the EGFP-TJ-Claudin5 mouse line, illustrating tight junctions at the arterial, venous, and capillary levels. Individual ECs are outlined with dashed lines for clarity. Scale bars: 10 µm.

(B) Proposed mechanism of capillary repair, involving neighboring EC extension. (Top) Time-lapse two-photon images taken at respective time points with zoomed-in insets. Teal and yellow shadings indicate neighboring ECs repairing the capillary within 24–48 h. (Bottom) Schematic highlighting individual ECs in different colors and tight junctions in black, showing how the neighboring ECs (teal and yellow EC in this example) gradually extend toward the lesion site (gray EC). Scale bar: 10 µm.

(C) Representative two-photon image series of sparse labeled EC (red arrowhead) in the EGFP-TJ-Claudin5 mouse. The arrowheads are pointing to ECs. Scale bar: 5 µm.

(D) Quantification of EC length pre and post extension ($N = 1$, $n = 5$). The red point represents the quantification of the illustrative example shown in (C).

(E) Schematic of VEGFR2-Akt-mTOR signaling pathway. VEGF binding to VEGFR2 activates phosphatidylinositol 3-kinase (PI3K)-Akt signaling. mTORC2 is involved in cytoskeletal remodeling and cellular elongation, while mTORC1 is involved in protein synthesis pathways and EC proliferation. DC101 blocks the VEGFR2 receptor, and Ku-0063794 is a dual mTOR inhibitor.

(F) Quantification of capillary repair after DC101 (left) and Ku-0063794 (right) treatment. Corresponding controls are shown in light shading within each pie chart. DC101: N = 5, n = 25; VEGFR2 isotype antibody: $N = 3$, $n = 17$. Ku-0063794: $N = 3$, $n = 10$; and vehicle control: $N = 3$, $n = 11$. N, number of animals; n, number of capillaries.

Please cite this article in press as: Condrau et al., Intrinsic endothelial remodeling drives brain capillary repair, Neuron (2026), https://doi.org/10.1016/j.neuron.2026.04.020

CellPress
OPEN ACCESS

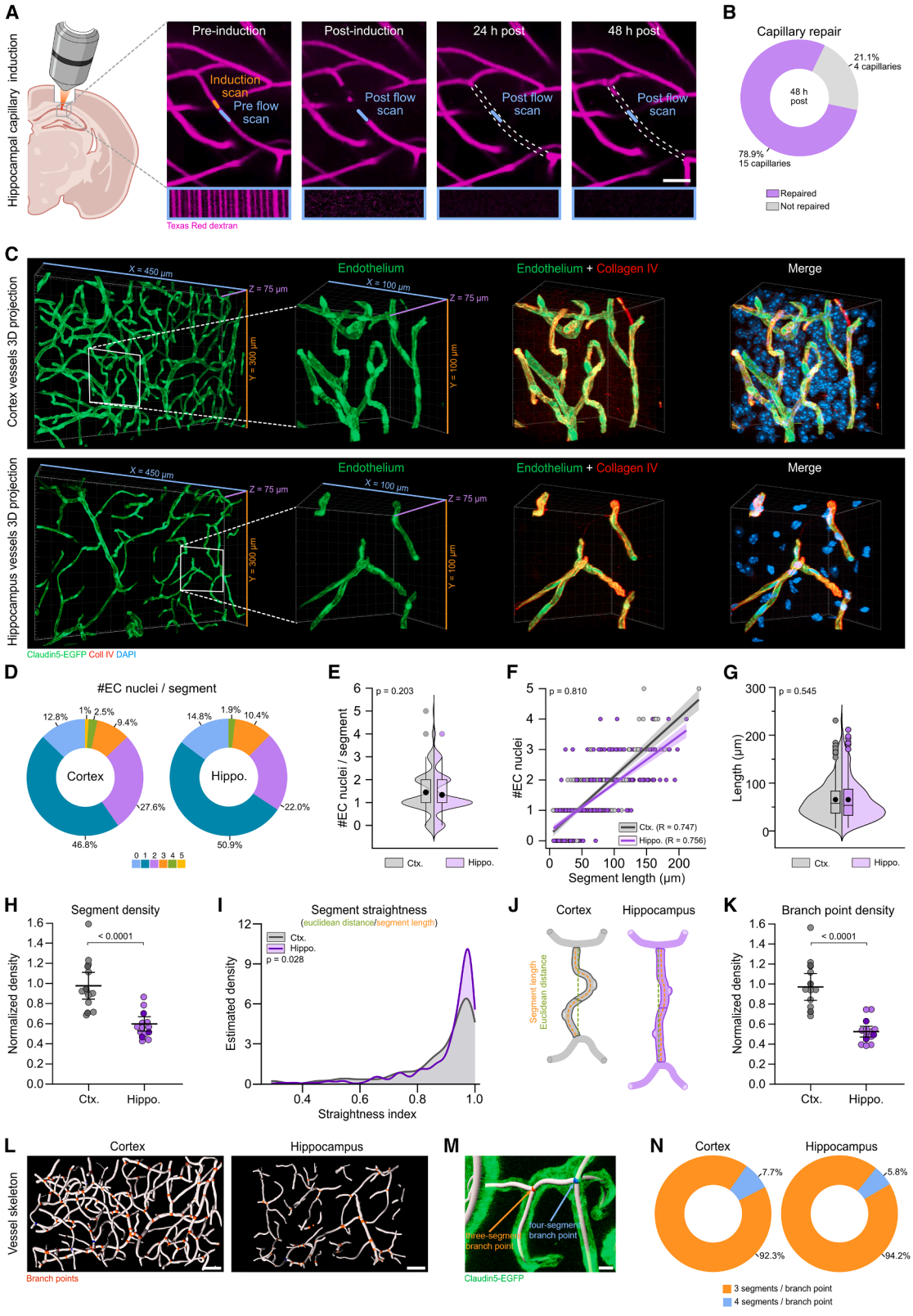

(legend on next page)

Please cite this article in press as: Condrau et al., Intrinsic endothelial remodeling drives brain capillary repair, Neuron (2026), https://doi.org/10.1016/j.neuron.2026.04.020

investigation of the effect of single EC death in the brain microvascular network. Our work provides a toolset to overcome this challenge and extend previous research to investigate the mechanisms of brain capillary repair following local EC injury.

Previous studies have been focusing on endothelial recovery in larger cerebral vessels showing vascular repair via EC proliferation.[45] In the scenario of a stroke, post-stroke reparative angiogenesis begins in the peri-infarct zone from pre-existing blood vessels, with ECs playing a crucial role in driving this process.[61] Notably, this response is guided and modulated by various angiogenic factors, particularly VEGF signaling, which is known to support EC survival, migration, and proliferation.[62]

Here, we demonstrate that, at the capillary level, when a single EC dies, the repair is driven by local extension of neighboring ECs rather than by EC proliferation. The extended ECs close the gap left by the lost EC within 24–48 h, thereby restoring capillary integrity and tissue perfusion. We show that inhibition of VEGFR2 signaling attenuates capillary repair at 24 and 48 h post-induction. Moreover, inhibition of mTOR signaling, and thereby cytoskeletal remodeling and EC elongation, also markedly reduced capillary repair at both time points, underscoring the essential role of actin remodeling in enabling EC extension. Previous studies demonstrated that VEGFR2 inhibition or endothelial-specific VEGFR2 knockdown preserves capillaries following microsphere-induced obstructions or capillary stalls,[20,25] highlighting a role for VEGF signaling in capillary recanalization and flow restoration. In contrast, ECgo induces localized EC loss rather than a hemodynamic stall, representing a distinct type of microvascular perturbation. Accordingly, our findings do not contradict prior work but instead address a different aspect of capillary maintenance. It is likely that ECs use VEGF signaling to extend their cellular membrane and ensure capillary regeneration.

Our findings align with previous work showing a comparable endothelial-mediated repair mechanism in the skin microvasculature.[48] In this instance, local EC ablation prompted neighboring ECs to elongate or migrate toward the injury site, with no evidence of EC proliferation or replacement. Collectively, these findings suggest that EC plasmalemmal extension might be a potential mechanism for capillary repair across different organs.

Interestingly, EC extension capacity in the brain cortex appears to have a spatiotemporal limit, and consistent with this, the deletion of 2 neighboring ECs reduced and delayed capillary repair in our model. Future studies will be required to quantitatively assess the extension limit of ECs in different brain regions and disease conditions.

Although ECs are in close contact with pericytes and astrocytes, we show that ECs can repair a targeted capillary segment independently of astrocyte or pericyte coverage. Parenchymal microglia have been proven to react locally to a microvascular insult by extending their processes toward sites of injury,[63] and prior studies have reported a functional role for microglia in vascular repair.[64–66] A previous study by Mehina et al.[65] showed that microglia play a crucial role in capillary repair following laser-induced vessel rupture and microbleeds, and that microglial depletion reduced capillary repair by ~18%.[65] The injury in our model differs in that ECgo induces highly localized EC loss. Notably, depletion of microglia using the PLX3397 diet did not reduce capillary repair capacity. It is likely that the magnitude and functional significance of the microglial response are

Figure 6. Hippocampal capillaries exhibit reduced repair despite architectural similarity to cortical capillaries

(A) Transcortical window preparation for *in vivo* hippocampal imaging using two-photon microscopy. Maximum intensity two-photon 20-μm z projections of hippocampal capillaries at different time points with corresponding flow scans to the right (x, distance; t, time). Dashed lines mark the former location of the capillary 24 and 48 h post-induction. Scale bar: 20 μm.

(B) Quantification of *in vivo* hippocampal capillary repair (78.9%) 48 h post-induction ($N = 3$ animals, $n = 19$ capillaries).

(C) Representative histological vessel 3D projections in the cortex (top) and hippocampus (bottom). Dimensions of both 3D overview boxes are 450 × 300 × 75 μm (*x*, *y*, and *z*; tick marks = 6 μm) and those of the zoom-ins are 100 × 100 × 75 μm (*x*, *y*, and *z*; tick marks = 2 μm).

(D) Histological quantification showing the distribution of ECs per capillary segment (only internodal segments with a mean diameter ≤ 5.2 μm are included) in the cortex (left) and hippocampus (right). $N = 3$ animals; $n_{ctx} = 203$, $n_{hippo} = 318$ segments.

(E) Histological quantification of number of ECs per capillary segment in the cortex and hippocampus ($N = 3$ animals; $n_{ctx} = 203$, $n_{hippo} = 318$ segments; $W = 34{,}260$; $p = 0.203$, unpaired Mann-Whitney U test). Black dots represent the mean.

(F) Correlation of capillary segment length and number of ECs per segment in the cortex and hippocampus in histological data ($N = 3$ animals; $n_{ctx} = 203$, $n_{hippo} = 318$ segments; $rho_{ctx} = 0.747$, $rho_{hippo} = 0.756$; $p = 0.810$, Spearman Rank correlation with Fisher's Z test).

(G) Histological quantification of individual capillary segment length in the cortex and hippocampus ($N = 3$; $n_{ctx} = 203$, $n_{hippo} = 318$ segments; estimate = −0.066 ± 0.11; $t = -0.606$; $p = 0.545$, generalized mixed model with Gamma distribution). Black colored dots represent the mean; horizontal bars represent the median.

(H) Normalized vessel segment (included are all vessels) density plot of histological slices in the cortex and hippocampus ($N = 3$ animals; $n_{ctx} = 3{,}357$, $n_{hippo} = 1{,}626$ segments; $t(19) = 6.053$; $p < 0.0001$, linear mixed model fit by REML, mean ± SEM).

(I) Superimposed estimated density plot of capillary segment straightness in cortical and hippocampal slices ($N = 3$ animals; $n_{ctx} = 203$, $n_{hippo} = 318$ segments; estimate = 0.055 ± 0.025; $t = 2.196$; $p = 0.028$, generalized linear mixed model with gamma distribution). Low straightness index, tortuous morphology; high straightness index, straight morphology.

(J) Schematic illustrating capillary segment length (orange) vs. Euclidean distance (green) in cortical (left) and hippocampal (right) capillaries, illustrating the straighter architecture of hippocampal capillaries.

(K) Normalized branch point density plot of histological slices in the cortex and hippocampus ($N = 3$ animals; $n_{ctx} = 1{,}654$, $n_{hippo} = 707$ branch points; $t(19) = 6.856$; $p < 0.0001$, linear mixed model fit by REML, mean ± SEM).

(L) Representative vessel skeleton of cortical (left) and hippocampal (right) slices. Red point, branch points consisting of 3 segments; blue, branch points consisting of 4 segments. Scale bar: 50 μm.

(M) Representative capillary skeleton showing a three-segment branch point (red) and a four-segment branch point (blue). The arrows are pointing to branch points. Scale bar: 5 μm.

(N) Histological quantification of percentage of three-segment branch points and four-segment branch points in the cortex (left) and hippocampus (right). $N = 3$ animals, $n_{ctx} = 1{,}654$, $n_{hippo} = 707$ branch points.

determined by the severity of the injury. Altogether, these studies suggest that extensive vascular damage elicits sustained microglial responses that promote vascular repair, whereas localized endothelial injury provokes a milder response that is dispensable for capillary restoration.

We consistently observed that repaired capillary segments retained their original shape, suggesting that ECs align along the basement membrane (BM).[67] The BM likely facilitates the restoration of the capillary's structure, acting as a scaffold for EC extension. This idea is supported by previous work demonstrating endothelial migration along residual vascular BM following skeletal muscle infarction.[68] Indeed, if ECs do not repopulate the BM, the tubes can collapse, forming acellular, non-perfused string vessels. We occasionally observed string vessels in our study, and they are commonly found in the post-mortem brains of Alzheimer's patients, where they correlate with capillary rarefaction.[59–62,69,70] Taken together, these observations highlight the importance of mechanisms that preserve capillary integrity following focal endothelial loss. Despite continuous exposure to mechanical and metabolic stressors, ECs are integral in maintaining capillary integrity throughout life.[14,71,72] While not designed to model a specific disease, ECgo provides a framework for investigating capillary maintenance and repair, defining the limits of microvascular resilience to focal injury.

The hippocampus, a brain area critical for learning and memory, is known to be particularly vulnerable to microvascular injury.[47,63–65] Microvascular dysfunction is also a hallmark of neurodegenerative disorders, including AD,[52,73] and has been implicated in early hippocampal tissue damage observed in the initial stages of AD.[74,75] Prior reports highlighted differences between the hippocampus and cortex in terms of oxygenation and neurovascular coupling, suggesting that these differences are due to a reduced hippocampal vascular density.[50,76] Our study extends the current knowledge by showing that EC-autonomous repair also differs in the hippocampal capillary network. Similarly, previous studies demonstrated that ECs from different brain regions exhibit heterogeneity at cellular, transcriptional, and functional levels.[31,77–80] Future studies investigating regional variations in EC-autonomous repair will advance our understanding of brain vascular maintenance and repair across brain regions.

Overall, this study provides the first detailed characterization of brain capillary EC remodeling in the context of microvascular repair. These results may offer new insights into the mechanisms underlying capillary rarefaction in neurodegenerative disorders.

RESOURCE AVAILABILITY

Lead contact

Further information and requests for resources and reagents should be directed to and will be fulfilled by the lead contact, Bruno Weber (bweber@pharma.uzh.ch).

Materials availability

This study did not generate any new, unique reagents. Ps2P was developed by the group of Sergei A. Vinogradov and has been described previously.[32]

Data and code availability

- All data reported in this paper will be shared by the lead contact upon request.
- All original code has been deposited at Zenodo and is publicly available at https://doi.org/10.5281/zenodo.19471983 as of the date of publication.
- Any additional information required to reanalyze the data reported in this paper is available from the lead contact upon request.

ACKNOWLEDGMENTS

We thank all present and former laboratory members for their contributions to this project. We thank D. Agalliu for generously sharing the EGFP-TJ-Claudin5 mice with us. We want to express our thanks to C. Betsholtz for providing Claudin5-EGFP mice and Lubor Borsig for the Cx3cr1-GFP mice. We want to thank A. Keller for the fruitful discussions and feedback on the manuscript. We thank J. Körbelin for the supply of the BR1-AAV plasmid. We are grateful for continuous support from S. Weber, H. Osswald, N. Binini, and A. Siebert.

M.H. was supported by the UZH Candoc Postdoc Grant (FK-22-048), the Swiss National Science Foundation (SNSF) grant (PZ00′3_216616/1), and the Olga Mayenfisch Foundation (2024). B.W. was supported by grants from the SNSF (grant numbers 310030_219656 and 310030_182703). S.A.V. acknowledges support of the grants EB028941 and EB033877 from the National Institutes of Health.

AUTHOR CONTRIBUTIONS

Conceptualization, J.C., C.G., M.T.W., M.E.A., and B.W.; investigation, J.C., C.G., M.T.W., L.H., E.E., H.S.Z., A.v.F.-C., and G.E.; methodology, J.C., E.E., L.R., S.R.A., T.V.E., T.T., S.A.V., and B.W.; formal analysis, J.C., L.H., and E.E.; visualization, J.C., C.G., L.H., M.T.W., M.E.A., and B.W.; writing – original draft, J.C., C.G., M.T.W., M.E.A., and B.W.; writing – review & editing, all authors; supervision, B.W., M.E.A., S.A.V., and M.T.W.; and resources, B.W., M.E.A., and S.A.V.

DECLARATION OF INTERESTS

M.H. served on scientific advisory boards of Biogen, Merck Serono, Alexion, Roche, and Horizon Therapeutics (Amgen); received speaker's honoraria from Biogen; and received travel funding from Roche. Her institution received an unrestricted research grant from Roche. J.L.B. has reported receiving consulting fees from AbbVie, Alexion, Antigenomycs, BeiGene, Chugai, Clene Nanomedicine, EMD Serono, Genentech, Genzyme, Horizon Therapeutics, Mitsubishi Tanabe Pharma, MedImmune/Viela Bio, Novartis, Reistone BioPharma, Roche, and TG Therapeutics. In addition, J.L.B. has reported research grants from Novartis, Mallinckrodt, and Alexion. J.L.B. also holds a patent for aquaporumab.

STAR★METHODS

Detailed methods are provided in the online version of this paper and include the following:

- KEY RESOURCES TABLE
- EXPERIMENTAL MODEL AND STUDY PARTICIPANT DETAILS
  - Study approval and ethics statement
  - Animals
- METHOD DETAILS
  - Head plate surgery
  - Craniotomy and cortical window implantation
  - Transcortical window implantation
  - *In vivo* two-photon imaging
  - Imaging of cerebral vasculature
  - Blood flow and vascular diameter measurements
  - Induction of EC damage
  - Quantification of microglia responses
  - Pharmacological microglia depletion
  - Local astrocyte ablation
  - Optical pericyte ablation

SUPPLEMENTAL INFORMATION

Supplemental information can be found online at https://doi.org/10.1016/j.neuron.2026.04.020.

Received: November 6, 2025
Revised: February 27, 2026
Accepted: April 9, 2026

REFERENCES

1. Jespersen, S.N., and Østergaard, L. (2012). The Roles of Cerebral Blood Flow, Capillary Transit Time Heterogeneity, and Oxygen Tension in Brain Oxygenation and Metabolism. J. Cereb. Blood Flow Metab. *32*, 264–277. https://doi.org/10.1038/jcbfm.2011.153.
2. Drew, P.J., Shih, A.Y., and Kleinfeld, D. (2011). Fluctuating and sensory-induced vasodynamics in rodent cortex extend arteriole capacity. Proc. Natl. Acad. Sci. USA *108*, 8473–8478. https://doi.org/10.1073/pnas.1100428108.
3. Kleinfeld, D., Mitra, P.P., Helmchen, F., and Denk, W. (1998). Fluctuations and stimulus-induced changes in blood flow observed in individual capillaries in layers 2 through 4 of rat neocortex. Proc. Natl. Acad. Sci. USA *95*, 15741–15746. https://doi.org/10.1073/pnas.95.26.15741.
4. Villringer, A., Haberl, R.L., Dirnagl, U., Anneser, F., Verst, M., and Einhäupl, K.M. (1989). Confocal laser microscopy to study microcirculation on the rat brain surface in vivo. Brain Res. *504*, 159–160. https://doi.org/10.1016/0006-8993(89)91616-8.
5. Blinder, P., Shih, A.Y., Rafie, C., and Kleinfeld, D. (2010). Topological basis for the robust distribution of blood to rodent neocortex. Proc. Natl. Acad. Sci. USA *107*, 12670–12675. https://doi.org/10.1073/pnas.1007239107.
6. Blinder, P., Tsai, P.S., Kaufhold, J.P., Knutsen, P.M., Suhl, H., and Kleinfeld, D. (2013). The cortical angiome: an interconnected vascular network with noncolumnar patterns of blood flow. Nat. Neurosci. *16*, 889–897. https://doi.org/10.1038/nn.3426.
7. Yu, Q.J., Tao, H., Wang, X., and Li, M.C. (2015). Targeting brain microvascular endothelial cells: a therapeutic approach to neuroprotection against stroke. Neural Regen. Res. *10*, 1882–1891. https://doi.org/10.4103/1673-5374.170324.
8. Abbott, N.J. (2002). Astrocyte–endothelial interactions and blood–brain barrier permeability. J. Anat. *200*, 629–638. https://doi.org/10.1046/j.1469-7580.2002.00064.x.
9. Daneman, R. (2012). The blood-brain barrier in health and disease. Ann. Neurol. *72*, 648–672. https://doi.org/10.1002/ana.23648.
10. Kadry, H., Noorani, B., and Cucullo, L. (2020). A blood–brain barrier overview on structure, function, impairment, and biomarkers of integrity. Fluids Barriers CNS *17*, 69. https://doi.org/10.1186/s12987-020-00230-3.
11. Armulik, A., Abramsson, A., and Betsholtz, C. (2005). Endothelial/Pericyte Interactions. Circ. Res. *97*, 512–523. https://doi.org/10.1161/01.RES.0000182903.16652.d7.
12. Galea, I. (2021). The blood–brain barrier in systemic infection and inflammation. Cell. Mol. Immunol. *18*, 2489–2501. https://doi.org/10.1038/s41423-021-00757-x.
13. Jufri, N.F., Mohamedali, A., Avolio, A., and Baker, M.S. (2015). Mechanical stretch: physiological and pathological implications for human vascular endothelial cells. Vasc. Cell *7*, 8. https://doi.org/10.1186/s13221-015-0033-z.
14. Peng, Z., Shu, B., Zhang, Y., and Wang, M. (2019). Endothelial Response to Pathophysiological Stress. Arterioscler. Thromb. Vasc. Biol. *39*, e233–e243. https://doi.org/10.1161/ATVBAHA.119.312580.
15. Bonney, S.K., Coelho-Santos, V., Huang, S.F., Takeno, M., Kornfeld, J., Keller, A., and Shih, A.Y. (2022). Public Volume Electron Microscopy Data: An Essential Resource to Study the Brain Microvasculature. Front. Cell Dev. Biol. *10*, 849469. https://doi.org/10.3389/fcell.2022.849469.
16. McDonald, A.I., Shirali, A.S., Aragón, R., Ma, F., Hernandez, G., Vaughn, D.A., Mack, J.J., Lim, T.Y., Sunshine, H., Zhao, P., et al. (2018). Endothelial Regeneration of Large Vessels Is a Biphasic Process Driven by Local Cells with Distinct Proliferative Capacities. Cell Stem Cell *23*, 210–225.e6. https://doi.org/10.1016/j.stem.2018.07.011.
17. Evans, C.E., Iruela-Arispe, M.L., and Zhao, Y.-Y. (2021). Mechanisms of Endothelial Regeneration and Vascular Repair and Their Application to Regenerative Medicine. Am. J. Pathol. *191*, 52–65. https://doi.org/10.1016/j.ajpath.2020.10.001.
18. Hess, D.C., Hill, W.D., Martin-Studdard, A., Carroll, J., Brailer, J., and Carothers, J. (2002). Bone marrow as a source of endothelial cells and NeuN-expressing cells After stroke. Stroke *33*, 1362–1368. https://doi.org/10.1161/01.str.0000014925.09415.c3.
19. Li, L., Welser, J.V., Dore-Duffy, P., del del Zoppo, G.J., LaManna, J.C., and Milner, R. (2010). In the hypoxic central nervous system, endothelial cell proliferation is followed by astrocyte activation, proliferation, and increased expression of the α6β4 integrin and dystroglycan. Glia *58*, 1157–1167. https://doi.org/10.1002/glia.20995.
20. Ali, M., Falkenhain, K., Njiru, B.N., Murtaza-Ali, M., Ruiz-Uribe, N.E., Haft-Javaherian, M., Catchers, S., Nishimura, N., Schaffer, C.B., and Bracko, O. (2022). VEGF signalling causes stalls in brain capillaries and reduces cerebral blood flow in Alzheimer's mice. Brain *145*, 1449–1463. https://doi.org/10.1093/brain/awab387.
21. El Amki, M., Glück, C., Binder, N., Middleham, W., Wyss, M.T., Weiss, T., Meister, H., Luft, A., Weller, M., Weber, B., et al. (2020). Neutrophils Obstructing Brain Capillaries Are a Major Cause of No-Reflow in Ischemic Stroke. Cell Rep. *33*, 108260. https://doi.org/10.1016/j.celrep.2020.108260.
22. Cruz Hernández, J.C., Bracko, O., Kersbergen, C.J., Muse, V., Haft-Javaherian, M., Berg, M., Park, L., Vinarcsik, L.K., Ivasyk, I., Rivera, D.A., et al. (2019). Neutrophil adhesion in brain capillaries reduces cortical blood flow and impairs memory function in Alzheimer's disease mouse models. Nat. Neurosci. *22*, 413–420. https://doi.org/10.1038/s41593-018-0329-4.
23. Erdener, Ş.E., Tang, J., Kılıç, K., Postnov, D., Giblin, J.T., Kura, S., Chen, I.A., Vayisoğlu, T., Sakadžić, S., Schaffer, C.B., et al. (2021). Dynamic capillary stalls in reperfused ischemic penumbra contribute to injury: A hyperacute role for neutrophils in persistent traffic jams. J. Cereb. Blood Flow Metab. *41*, 236–252. https://doi.org/10.1177/0271678X20914179.
24. Erdener, Ş.E., Tang, J., Sajjadi, A., Kılıç, K., Kura, S., Schaffer, C.B., and Boas, D.A. (2019). Spatio-temporal dynamics of cerebral capillary segments with stalling red blood cells. J. Cereb. Blood Flow Metab. *39*, 886–900. https://doi.org/10.1177/0271678X17743877.
25. Reeson, P., Choi, K., and Brown, C.E. (2018). VEGF signaling regulates the fate of obstructed capillaries in mouse cortex. eLife *7*, e33670. https://doi.org/10.7554/eLife.33670.
26. Schager, B., and Brown, C.E. (2020). Susceptibility to capillary plugging can predict brain region specific vessel loss with aging. J. Cereb. Blood Flow Metab. *40*, 2475–2490. https://doi.org/10.1177/0271678X19895245.
27. Salmina, A.B., Inzhutova, A.I., Malinovskaya, N.A., and Petrova, M.M. (2010). Endothelial Dysfunction and Repair in Alzheimer-Type Neurodegeneration: Neuronal and Glial Control. J. Alzheimers Dis. *22*, 17–36. https://doi.org/10.3233/JAD-2010-091690.

28. Bai, T., Yu, S., and Feng, J. (2022). Advances in the Role of Endothelial Cells in Cerebral Small Vessel Disease. Front. Neurol. *13*, 861714. https://doi.org/10.3389/fneur.2022.861714.

29. Sweeney, M.D., Sagare, A.P., and Zlokovic, B.V. (2018). Blood–brain barrier breakdown in Alzheimer disease and other neurodegenerative disorders. Nat. Rev. Neurol. *14*, 133–150. https://doi.org/10.1038/nrneurol.2017.188.

30. Kelleher, R.J., and Soiza, R.L. (2013). Evidence of endothelial dysfunction in the development of Alzheimer's disease: Is Alzheimer's a vascular disorder? Am. J. Cardiovasc. Dis. *3*, 197–226.

31. Bryant, A., Li, Z., Jayakumar, R., Serrano-Pozo, A., Woost, B., Hu, M., Woodbury, M.E., Wachter, A., Lin, G., Kwon, T., et al. (2023). Endothelial Cells Are Heterogeneous in Different Brain Regions and Are Dramatically Altered in Alzheimer's Disease. J. Neurosci. *43*, 4541–4557. https://doi.org/10.1523/JNEUROSCI.0237-23.2023.

32. Condrau, J., Allu, S.R., Esipova, T.V., Erlebach, E., Wyss, M.T., Glück, C., Ravotto, L., Troxler, T., Villa, M., Ceroni, P., et al. (2026). ECgo: All-Optical Induction of Single Endothelial Cell Injury and Capillary Occlusion in the Brain. Proc. Natl. Acad. Sci. USA, in press. https://doi.org/10.1073/pnas.2513515123.

33. Nishimura, N., Schaffer, C.B., Friedman, B., Tsai, P.S., Lyden, P.D., and Kleinfeld, D. (2006). Targeted insult to subsurface cortical blood vessels using ultrashort laser pulses: three models of stroke. Nat. Methods *3*, 99–108. https://doi.org/10.1038/nmeth844.

34. Shih, A.Y., Blinder, P., Tsai, P.S., Friedman, B., Stanley, G., Lyden, P.D., and Kleinfeld, D. (2013). The smallest stroke: occlusion of one penetrating vessel leads to infarction and a cognitive deficit. Nat. Neurosci. *16*, 55–63. https://doi.org/10.1038/nn.3278.

35. Paone, S., Baxter, A.A., Hulett, M.D., and Poon, I.K.H. (2019). Endothelial cell apoptosis and the role of endothelial cell-derived extracellular vesicles in the progression of atherosclerosis. Cell. Mol. Life Sci. *76*, 1093–1106. https://doi.org/10.1007/s00018-018-2983-9.

36. Jung, K.-H., Chu, K., Lee, S.-T., Park, H.-K., Bahn, J.-J., Kim, D.-H., Kim, J.-H., Kim, M., Kun Lee, S., and Roh, J.-K. (2009). Circulating endothelial microparticles as a marker of cerebrovascular disease. Ann. Neurol. *66*, 191–199. https://doi.org/10.1002/ana.21681.

37. Bergers, G., and Song, S. (2005). The role of pericytes in blood-vessel formation and maintenance. Neuro. Oncol *7*, 452–464. https://doi.org/10.1215/S1152851705000232.

38. Brown, L.S., Foster, C.G., Courtney, J.M., King, N.E., Howells, D.W., and Sutherland, B.A. (2019). Pericytes and Neurovascular Function in the Healthy and Diseased Brain. Front. Cell. Neurosci. *13*, 282. https://doi.org/10.3389/fncel.2019.00282.

39. Kisler, K., Nikolakopoulou, A.M., and Zlokovic, B.V. (2021). Microglia have a grip on brain microvasculature. Nat. Commun. *12*, 5290. https://doi.org/10.1038/s41467-021-25595-3.

40. Manu, D.R., Slevin, M., Barcutean, L., Forro, T., Boghitoiu, T., and Balasa, R. (2023). Astrocyte Involvement in Blood–Brain Barrier Function: A Critical Update Highlighting Novel, Complex, Neurovascular Interactions. Int. J. Mol. Sci. *24*, 17146. https://doi.org/10.3390/ijms242417146.

41. Elmore, M.R.P., Najafi, A.R., Koike, M.A., Dagher, N.N., Spangenberg, E.E., Rice, R.A., Kitazawa, M., Matusow, B., Nguyen, H., West, B.L., et al. (2014). Colony-Stimulating Factor 1 Receptor Signaling Is Necessary for Microglia Viability, Unmasking a Microglia Progenitor Cell in the Adult Brain. Neuron *82*, 380–397. https://doi.org/10.1016/j.neuron.2014.02.040.

42. Herwerth, M., Wyss, M.T., Schmid, N.B., Condrau, J., Ravotto, L., Mateos Melero, J.M., Kaech, A., Bredell, G., Thomas, C., Stadelmann, C., et al. (2024). Astrocytes adopt a progenitor-like migratory strategy for regeneration in adult brain.. Preprint at bioRxiv. https://doi.org/10.1101/2024.05.18.594292.

43. Bonney, S.K., Nielson, C.D., Sosa, M.J., Bonnar, O., and Shih, A.Y. (2024). Capillary regression leads to sustained local hypoperfusion by inducing constriction of upstream transitional vessels. Proc. Natl. Acad. Sci. USA *121*, e2321021121. https://doi.org/10.1073/pnas.2321021121.

44. Nielson, C.D., and Shih, A.Y. (2022). In vivo Single Cell Optical Ablation of Brain Pericytes. Front. Neurosci. *16*, 900761. https://doi.org/10.3389/fnins.2022.900761.

45. Itoh, Y., Toriumi, H., Yamada, S., Hoshino, H., and Suzuki, N. (2010). Resident Endothelial Cells Surrounding Damaged Arterial Endothelium Reendothelialize the Lesion. Arterioscler. Thromb. Vasc. Biol. *30*, 1725–1732. https://doi.org/10.1161/ATVBAHA.110.207365.

46. Knowland, D., Arac, A., Sekiguchi, K.J., Hsu, M., Lutz, S.E., Perrino, J., Steinberg, G.K., Barres, B.A., Nimmerjahn, A., and Agalliu, D. (2014). Stepwise Recruitment of Transcellular and Paracellular Pathways Underlies Blood-Brain Barrier Breakdown in Stroke. Neuron *82*, 603–617. https://doi.org/10.1016/j.neuron.2014.03.003.

47. Körbelin, J., Dogbevia, G., Michelfelder, S., Ridder, D.A., Hunger, A., Wenzel, J., Seismann, H., Lampe, M., Bannach, J., Pasparakis, M., et al. (2016). A brain microvasculature endothelial cell-specific viral vector with the potential to treat neurovascular and neurological diseases. EMBO Mol. Med. *8*, 609–625. https://doi.org/10.15252/emmm.201506078.

48. Kam, C.Y., Singh, I.D., Gonzalez, D.G., Matte-Martone, C., Solá, P., Solanas, G., Bonjoch, J., Marsh, E., Hirschi, K.K., and Greco, V. (2023). Mechanisms of skin vascular maturation and maintenance captured by longitudinal imaging of live mice. Cell *186*, 2345–2360.e16. https://doi.org/10.1016/j.cell.2023.04.017.

49. Tsuji-Tamura, K., and Ogawa, M. (2018). Dual inhibition of mTORC1 and mTORC2 perturbs cytoskeletal organization and impairs endothelial cell elongation. Biochem. Biophys. Res. Commun. *497*, 326–331. https://doi.org/10.1016/j.bbrc.2018.02.080.

50. Shaw, K., Bell, L., Boyd, K., Grijseels, D.M., Clarke, D., Bonnar, O., Crombag, H.S., and Hall, C.N. (2021). Neurovascular coupling and oxygenation are decreased in hippocampus compared to neocortex because of microvascular differences. Nat. Commun. *12*, 3190. https://doi.org/10.1038/s41467-021-23508-y.

51. Ji, X., Ferreira, T., Friedman, B., Liu, R., Liechty, H., Bas, E., Chandrashekar, J., and Kleinfeld, D. (2021). Brain microvasculature has a common topology with local differences in geometry that match metabolic load. Neuron *109*, 1168–1187.e13. https://doi.org/10.1016/j.neuron.2021.02.006.

52. Johnson, A.C. (2023). Hippocampal Vascular Supply and Its Role in Vascular Cognitive Impairment. Stroke *54*, 673–685. https://doi.org/10.1161/STROKEAHA.122.038263.

53. Davidson, T.L., and Stevenson, R.J. (2024). Vulnerability of the Hippocampus to Insults: Links to Blood–Brain Barrier Dysfunction. Int. J. Mol. Sci. *25*, 1991. https://doi.org/10.3390/ijms25041991.

54. Dombeck, D.A., Harvey, C.D., Tian, L., Looger, L.L., and Tank, D.W. (2010). Functional imaging of hippocampal place cells at cellular resolution during virtual navigation. Nat. Neurosci. *13*, 1433–1440. https://doi.org/10.1038/nn.2648.

55. Kirst, C., Skriabine, S., Vieites-Prado, A., Topilko, T., Bertin, P., Gerschenfeld, G., Verny, F., Topilko, P., Michalski, N., Tessier-Lavigne, M., et al. (2020). Mapping the Fine-Scale Organization and Plasticity of the Brain Vasculature. Cell *180*, 780–795.e25. https://doi.org/10.1016/j.cell.2020.01.028.

56. Tsai, P.S., Kaufhold, J.P., Blinder, P., Friedman, B., Drew, P.J., Karten, H.J., Lyden, P.D., and Kleinfeld, D. (2009). Correlations of Neuronal and Microvascular Densities in Murine Cortex Revealed by Direct Counting and Colocalization of Nuclei and Vessels. J. Neurosci. *29*, 14553–14570. https://doi.org/10.1523/JNEUROSCI.3287-09.2009.

57. Wong, B.W., Marsch, E., Treps, L., Baes, M., and Carmeliet, P. (2017). Endothelial cell metabolism in health and disease: impact of hypoxia. EMBO J. *36*, 2187–2203. https://doi.org/10.15252/embj.201696150.

58. Fukuda, M., Matsumura, T., Suda, T., and Hirase, H. (2022). Depth-targeted intracortical microstroke by two-photon photothrombosis in rodent brain. Neurophotonics *9*, 021910. https://doi.org/10.1117/1.NPh.9.2.021910.

59. Delafontaine-Martel, P., Zhang, C., Lu, X., Damseh, R., Lesage, F., and Marchand, P.J. (2023). Targeted capillary photothrombosis via multi-photon excitation of Rose Bengal. J. Cereb. Blood Flow Metab. *43*, 1713–1725. https://doi.org/10.1177/0271678X231151560.

60. Zhu, L., Wang, M., Liu, Y., Fu, P., Zhang, W., Zhang, H., Roe, A.W., and Xi, W. (2023). Single-microvessel occlusion produces lamina-specific microvascular flow vasodynamics and signs of neurodegenerative change. Cell Rep. *42*, 112469. https://doi.org/10.1016/j.celrep.2023.112469.

61. Freitas-Andrade, M., Raman-Nair, J., and Lacoste, B. (2020). Structural and Functional Remodeling of the Brain Vasculature Following Stroke. Front. Physiol. *11*, 948. https://doi.org/10.3389/fphys.2020.00948.

62. Marti, H.J.H., Bernaudin, M., Bellail, A., Schoch, H., Euler, M., Petit, E., and Risau, W. (2000). Hypoxia-Induced Vascular Endothelial Growth Factor Expression Precedes Neovascularization after Cerebral Ischemia. Am. J. Pathol. *156*, 965–976. https://doi.org/10.1016/S0002-9440(10)64964-4.

63. Davalos, D., Grutzendler, J., Yang, G., Kim, J.V., Zuo, Y., Jung, S., Littman, D.R., Dustin, M.L., and Gan, W.-B. (2005). ATP mediates rapid microglial response to local brain injury in vivo. Nat. Neurosci. *8*, 752–758. https://doi.org/10.1038/nn1472.

64. Taylor, S., Mehina, E., White, E., Reeson, P., Yongblah, K., Doyle, K.P., and Brown, C.E. (2018). Suppressing Interferon-γ Stimulates Microglial Responses and Repair of Microbleeds in the Diabetic Brain. J. Neurosci. *38*, 8707–8722. https://doi.org/10.1523/JNEUROSCI.0734-18.2018.

65. Mehina, E.M.F., Taylor, S., Boghozian, R., White, E., Choi, S.E., Cheema, M.S., Korbelin, J., and Brown, C.E. (2021). Invasion of phagocytic Galectin 3 expressing macrophages in the diabetic brain disrupts vascular repair. Sci. Adv. *7*, eabg2712. https://doi.org/10.1126/sciadv.abg2712.

66. Halder, S.K., and Milner, R. (2019). A critical role for microglia in maintaining vascular integrity in the hypoxic spinal cord. Proc. Natl. Acad. Sci. USA *116*, 26029–26037. https://doi.org/10.1073/pnas.1912178116.

67. Thomsen, M.S., Routhe, L.J., and Moos, T. (2017). The vascular basement membrane in the healthy and pathological brain. J. Cereb. Blood Flow Metab. *37*, 3300–3317. https://doi.org/10.1177/0271678X17722436.

68. Vracko, R., and Benditt, E.P. (1972). Basal Lamina: The Scaffold for Orderly Cell Replacement. Observations on Regeneration of Injured Skeletal Muscle Fibers and Capillaries. J. Cell Biol. *55*, 406–419. https://doi.org/10.1083/jcb.55.2.406.

69. Brown, W.R. (2010). A Review of String Vessels or Collapsed, Empty Basement Membrane Tubes. J. Alzheimers Dis. *21*, 725–739. https://doi.org/10.3233/JAD-2010-100219.

70. Challa, V.R., Thore, C.R., Moody, D.M., Anstrom, J.A., and Brown, W.R. (2004). Increase of white matter string vessels in Alzheimer's disease. J. Alzheimers Dis. *6*, 379–83; discussion 443. https://doi.org/10.3233/JAD-2004-6404.

71. Keller, A. (2013). Breaking and building the wall: the biology of the blood-brain barrier in health and disease. Swiss Med. Wkly. *143*, w13892. https://doi.org/10.4414/smw.2013.13892.

72. Daneman, R., and Prat, A. (2015). The Blood–Brain Barrier. Cold Spring Harb. Perspect. Biol. *7*, a020412. https://doi.org/10.1101/cshperspect.a020412.

73. Buée, L., Hof, P.R., Bouras, C., Delacourte, A., Perl, D.P., Morrison, J.H., and Fillit, H.M. (1994). Pathological alterations of the cerebral microvasculature in Alzheimer's disease and related dementing disorders. Acta Neuropathol. *87*, 469–480. https://doi.org/10.1007/BF00294173.

74. Steinman, J., Sun, H.-S., and Feng, Z.-P. (2021). Microvascular Alterations in Alzheimer's Disease. Front. Cell. Neurosci. *14*, 618986. https://doi.org/10.3389/fncel.2020.618986.

75. Lee, H., Fu, J.F., Gaudet, K., Bryant, A.G., Price, J.C., Bennett, R.E., Johnson, K.A., Hyman, B.T., Hedden, T., Salat, D.H., et al. (2024). Aberrant vascular architecture in the hippocampus correlates with tau burden in mild cognitive impairment and Alzheimer's disease. J. Cereb. Blood Flow Metab. *44*, 787–800. https://doi.org/10.1177/0271678X231216144.

76. Hösli, L., Zuend, M., Bredell, G., Zanker, H.S., Porto de Oliveira, C.E., Saab, A.S., and Weber, B. (2022). Direct vascular contact is a hallmark of cerebral astrocytes. Cell Rep. *39*, 110599. https://doi.org/10.1016/j.celrep.2022.110599.

77. Montagne, A., Barnes, S.R., Sweeney, M.D., Halliday, M.R., Sagare, A.P., Zhao, Z., Toga, A.W., Jacobs, R.E., Liu, C.Y., Amezcua, L., et al. (2015). Blood-Brain Barrier Breakdown in the Aging Human Hippocampus. Neuron *85*, 296–302. https://doi.org/10.1016/j.neuron.2014.12.032.

78. Yang, A.C., Vest, R.T., Kern, F., Lee, D.P., Agam, M., Maat, C.A., Losada, P.M., Chen, M.B., Schaum, N., Khoury, N., et al. (2022). A human brain vascular atlas reveals diverse mediators of Alzheimer's risk. Nature *603*, 885–892. https://doi.org/10.1038/s41586-021-04369-3.

79. Matsuoka, R.L., Buck, L.D., Vajrala, K.P., Quick, R.E., and Card, O.A. (2022). Historical and current perspectives on blood endothelial cell heterogeneity in the brain. Cell. Mol. Life Sci. *79*, 372. https://doi.org/10.1007/s00018-022-04403-1.

80. Wälchli, T., Ghobrial, M., Schwab, M., Takada, S., Zhong, H., Suntharalingham, S., Vetiska, S., Gonzalez, D.R., Wu, R., Rehrauer, H., et al. (2024). Single-cell atlas of the human brain vasculature across development, adulthood and disease. Nature *632*, 603–613. https://doi.org/10.1038/s41586-024-07493-y.

81. Bennett, J.L., Lam, C., Kalluri, S.R., Saikali, P., Bautista, K., Dupree, C., Glogowska, M., Case, D., Antel, J.P., Owens, G.P., et al. (2009). Intrathecal pathogenic anti–aquaporin-4 antibodies in early neuromyelitis optica. Ann. Neurol. *66*, 617–629. https://doi.org/10.1002/ana.21802.

82. Stanczuk, L., Martinez-Corral, I., Ulvmar, M.H., Zhang, Y., Laviña, B., Fruttiger, M., Adams, R.H., Saur, D., Betsholtz, C., Ortega, S., et al. (2015). *cKit* Lineage Hemogenic Endothelium-Derived Cells Contribute to Mesenteric Lymphatic Vessels. Cell Rep. *10*, 1708–1721. https://doi.org/10.1016/j.celrep.2015.02.026.

83. Honkura, N., Richards, M., Laviña, B., Sáinz-Jaspeado, M., Betsholtz, C., and Claesson-Welsh, L. (2018). Intravital imaging-based analysis tools for vessel identification and assessment of concurrent dynamic vascular events. Nat. Commun. *9*, 2746. https://doi.org/10.1038/s41467-018-04929-8.

84. Cahoy, J.D., Emery, B., Kaushal, A., Foo, L.C., Zamanian, J.L., Christopherson, K.S., Xing, Y., Lubischer, J.L., Krieg, P.A., Krupenko, S.A., et al. (2008). A Transcriptome Database for Astrocytes, Neurons, and Oligodendrocytes: A New Resource for Understanding Brain Development and Function. J. Neurosci. *28*, 264–278. https://doi.org/10.1523/JNEUROSCI.4178-07.2008.

85. Pologruto, T.A., Sabatini, B.L., and Svoboda, K. (2003). ScanImage: Flexible software for operating laser scanning microscopes. Biomed. Eng. OnLine *2*, 13. https://doi.org/10.1186/1475-925X-2-13.

86. Barrett, M.J.P., Ferrari, K.D., Stobart, J.L., Holub, M., and Weber, B. (2018). CHIPS: an Extensible Toolbox for Cellular and Hemodynamic Two-Photon Image Analysis. Neuroinformatics *16*, 145–147. https://doi.org/10.1007/s12021-017-9344-y.

87. Drew, P.J., Blinder, P., Cauwenberghs, G., Shih, A.Y., and Kleinfeld, D. (2010). Rapid determination of particle velocity from space-time images using the Radon transform. J. Comput. Neurosci. *29*, 5–11. https://doi.org/10.1007/s10827-009-0159-1.

88. Schneider, C.A., Rasband, W.S., and Eliceiri, K.W. (2012). NIH Image to ImageJ: 25 years of image analysis. Nat. Methods *9*, 671–675. https://doi.org/10.1038/nmeth.2089.

89. Gong, S., Zheng, C., Doughty, M.L., Losos, K., Didkovsky, N., Schambra, U.B., Nowak, N.J., Joyner, A., Leblanc, G., Hatten, M.E., et al. (2003). A gene expression atlas of the central nervous system based on bacterial artificial chromosomes. Nature *425*, 917–925. https://doi.org/10.1038/nature02033.

90. Mayrhofer, J.M., Haiss, F., Haenni, D., Weber, S., Zuend, M., Barrett, M.J.P., Ferrari, K.D., Maechler, P., Saab, A.S., Stobart, J.L., et al. (2015). Design and performance of an ultra-flexible two-photon microscope for in vivo research. Biomed. Opt. Express *6*, 4228–4237. https://doi.org/10.1364/BOE.6.004228.

91. Zack, G.W., Rogers, W.E., and Latt, S.A. (1977). Automatic measurement of sister chromatid exchange frequency. J. Histochem. Cytochem. *25*, 741–753. https://doi.org/10.1177/25.7.70454.

92. Bisht, K., Okojie, K.A., Sharma, K., Lentferink, D.H., Sun, Y.Y., Chen, H.R., Uweru, J.O., Amancherla, S., Calcuttawala, Z., Campos-Salazar, A.B., et al. (2021). Capillary-associated microglia regulate vascular structure and function through PANX1-P2RY12 coupling in mice. Nat. Commun. *12*, 5289. https://doi.org/10.1038/s41467-021-25590-8.

93. Herwerth, M., Kenet, S., Schifferer, M., Winkler, A., Weber, M., Snaidero, N., Wang, M., Lohrberg, M., Bennett, J.L., Stadelmann, C., et al. (2022). A new form of axonal pathology in a spinal model of neuromyelitis optica. Brain *145*, 1726–1742. https://doi.org/10.1093/brain/awac079.

94. Stamenkovic, S., Schmid, F., Gurler, G., Abolmaali, F., Weitermann, N.A., Takasaki, K.T., Bonney, S.K., Sosa, M.J., Bennett, H.C., Kim, Y., et al. (2025). Impaired capillary-venous drainage contributes to gliosis and demyelination in mouse white matter during aging. Nat. Neurosci. *28*, 1868–1882. https://doi.org/10.1038/s41593-025-02023-z.

95. Bates, D., Mächler, M., Bolker, B., and Walker, S. (2015). Fitting Linear Mixed-Effects Models Using lme4. J. Stat. Softw. *67*, 1–48. https://doi.org/10.18637/jss.v067.i01.

96. Lenth, R.V. (2016). Least-Squares Means: The R Package lsmeans. J. Stat. Softw. *69*, 1–33. https://doi.org/10.18637/jss.v069.i01.

Please cite this article in press as: Condrau et al., Intrinsic endothelial remodeling drives brain capillary repair, Neuron (2026), https://doi.org/10.1016/j.neuron.2026.04.020

STAR★METHODS

KEY RESOURCES TABLE

REAGENT or RESOURCE	SOURCE	IDENTIFIER
Antibodies		
Rat anti-mouse VEGFR-2 (clone DC101)	Bio X Cell	Cat#BE0060; RRID: AB_1107766
Rat IgG1 isotype control	Bio X Cell	Cat#BE0088; RRID: AB_1107775
Goat anti-CD13 (1:400)	R and D Systems	Cat#AF2335; RRID: AB_2227288
Rabbit anti-Collagen IV (1:800)	Bio-Rad	Cat#2150-1470; RRID: AB_2082660
Cy3 anti-goat (1:700)	Jackson ImmunoResearch	Cat#705-165-003; RRID: AB_2340411
AF647 anti-rabbit (1:700)	Thermo Fisher Scientific	Cat#A32795; RRID: AB_2762835
AQP4-IgG (clone 7-5-53)	Bennett et al.[81]	N/A
Bacterial and virus strains		
AAV-BR1-shCAG-tdTomato	Körbelin et al.[47]	N/A
Chemicals, peptides, and recombinant proteins		
Buprenorphine (Temgesic)	Indivior Schweiz AG	Swissmedic#44100
Carprofen (Rimadyl)	Zoetis	Swissmedic#54375
Isoflurane (Attane)	Piramal Pharma	Swissmedic#56761
Fentanyl (Sintenyl)	Sintetica	Swissmedic#53987
Midazolam (Dormicum)	Cheplapharm	Swissmedic#44448
Medetomidine (Domitor)	Orion Pharma	Swissmedic#50590011
Flumazenil (Anexate)	Cheplapharm	Swissmedic#48280
Atipamezole (Revertor)	Virbac	Swissmedic#58701
Light-curing composite (Synergy D6 Flow)	Coltene AG	N/A
Histoacryl	B. Braun	N/A
Antibiotic ointment (Fucidin)	LEO Pharma	Swissmedic#46898
Gluma Comfort Bond	Heraeus Kulzer	N/A
Kodan forte	Schülke & Mayr AG	Swissmedic#44157
Ps2P	Condrau et al.[32]	N/A
Texas Red dextran (70 kDa)	Thermo Fisher Scientific	Cat#D1830
FITC dextran (70 kDa)	Sigma-Aldrich	Cat#46945
Qtracker655	Thermo Fisher Scientific	Cat#Q21021MP
Ku-0063794	MedChemExpress	Cat#HY-50710
Experimental models: Organisms/strains		
Mouse: C57BL/6J	Charles River	Cat#632C57BL/6J
Mouse: B6.129P-Cx3cr1<tm1Litt>/J	The Jackson Laboratory	JAX: 005582; RRID: IMSR_JAX:005582
Mouse: B6-Tg(Pdgfrb-Cre/ERT2)6096Rha x B6.CgGt(ROSA)26Sor<tm14(CAGtdTomato)Hze>/J	This paper	N/A
Mouse: B6.Cg-Tg(Cldn5-EGFP)Cbet/U	Stanczuk et al.[82]; Honkura et al.[83]	N/A
Mouse: C57BL/6-Tg(Tek-EGFP/Cldn5)15Drag	Knowland et al.[46]	N/A
Mouse: STOCK Tg(Aldh1l1.EGFP)OFC789Gsat/Mmucd	Cahoy et al.[84]	MMRRC: 011015-UCD
Software and algorithms		
ScanImage	Pologruto et al.[85]	https://docs.scanimage.org/About/Download+ScanImage.html
CHIPS toolbox for MatLab	Barrett et al.[86]	https://github.com/EIN-lab/CHIPS
MATLAB (version R2023b)	MathWorks	https://www.mathworks.com/products/matlab.html
Radon transform	Drew et al.[87]	https://neurophysics.ucsd.edu/software.php
R (version 4.4.2)	R Project	https://www.r-project.org

(*Continued on next page*)

Continued

REAGENT or RESOURCE	SOURCE	IDENTIFIER
Vascular Network Analysis	This paper	Zenodo: https://doi.org/10.5281/zenodo.19471983
ImageJ (version 2.1.0)	Schneider et al.[88]	https://imagej.net/ij/
Prism	GraphPad	https://www.graphpad.com
Imaris (version 10.2.0)	Oxford Instruments	https://imaris.oxinst.com
Other		
PLX3397 diet (CSF1R inhibitor)	Plexxikon	N/A
Human complement	Sigma-Aldrich	Cat#S1764

EXPERIMENTAL MODEL AND STUDY PARTICIPANT DETAILS

Study approval and ethics statement

The Swiss Animal Protection Law, Swiss Veterinary Office, Canton of Zurich (Animal Welfare Act of 16 December 2005 and Animal Protection Ordinance of 23 April 2008), and the local Cantonal Veterinary Office in Zurich (license ZH169/2017, ZH152/2021, ZH028/2023, ZH174/2021, ZH175/2025) approved the animal experiments in this study.

Animals

We utilized 2- to 8-month-old female and male mice. All mice were kept in an inverted 12:12-hour light-dark cycle animal husbandry, where ad libitum access to food and water was provided. Standard laboratory chow was used unless otherwise indicated. C57BL/6J mice (Charles River; Cat#632C57BL/6J) served as wild-type and control animals. For microglia studies, Cx3cr1-GFP reporter mice (B6.129P-Cx3cr1<tm1Litt>/J; Jackson Laboratory, Cat#005582) were utilized. To investigate the involvement of pericytes, we employed *Pdgfrb*-tdTomato mice (B6-Tg(Pdgfrb-Cre/ERT2)6096Rha x B6.CgGt(ROSA)26Sor<tm14(CAGtdTomato)Hze>/J). Studies on the endothelium were conducted using Claudin5-EGFP mice (B6.Cg-Tg(Cldn5-EGFP)Cbet/U)[82,83] or EGFP-TJ-Claudin5 (C57BL/6-Tg(Tek-EGFP/Cldn5)15Drag)[46] mice. The Aldh1l1-EGFP transgenic mouse line (STOCK Tg(Aldh1l1-EGFP)OFC789Gsat/Mmucd; ID: 011015-UCD)[89] was obtained from the Mutant Mouse Resource and Research Center (MMRRC) at University of California at Davis, an NIH-funded strain repository, and was donated to the MMRRC by Nathaniel Heintz, Ph.D., The Rockefeller University, GENSAT.

METHOD DETAILS

Head plate surgery

Buprenorphine (0.1 mg/kg; Temgesic; Indivior Schweiz AG; s.c.) was injected subcutaneously 30 min before the surgery started. Animals were anesthetized with isoflurane (5% for induction, 1.5% for maintenance provided by a face mask), with a flow rate of 300 ml/min of 100% oxygen and 600 ml/min of compressed air. The animal's body temperature was kept constant at 37 °C throughout the surgery using a heating mat. VitA Pos (Bausch + Lomb) eye ointment was applied to prevent dehydration and irritation of the eyes. The animal's head was shaved, and all hair was removed using depilatory cream (Veet). The scalp was cleaned and disinfected with Kodan (Schülke & Mayr AG). Subsequently, the animal was transferred to the stereotactic frame (Model 900; David Kopf Instruments), and the head was secured using ear bars. A midline incision of approximately 1.5 cm was made to expose the skull, and the periosteum was gently removed. A bonding agent (Gluma Comfort Bond; Heraeus Kulzer) was applied and polymerized with blue light (600 mW/cm^2; Demetron). A stainless-steel head plate, positioned centrally over the exposed skull (excluding the region over the left somatosensory cortex for the craniotomy), was secured using a light-curing composite (Synergy D6 Flow; Coltene AG). The skin lesion was sealed with acrylic glue (Histoacryl; B. Braun) and treated with antibiotic ointment (Neomycin; Cicatrex; Janssen-Cilag AG). Pre-warmed Ringerfundin (10 ml/kg; s.c.) was injected to prevent dehydration.

Craniotomy and cortical window implantation

Animals were anesthetized by a subcutaneous injection of a triple mix of the following drugs: Fentanyl (0.05 mg/kg; Sintenyl; Sintetica), medetomidine (0.5 mg/kg; Domitor; Orion Pharma) and midazolam (5 mg/kg; Dormicum; Cheplapharm). The animal's body temperature was kept constant at 37°C using a heating mat, and to prevent hypoxemia, 100% O_2 at a flow rate of 300 ml/min was provided via a face mask. A 4x4 mm craniotomy was performed over the left somatosensory cortex using a dental driller (H-4-002HP; Rotatec GmbH). A 3x3 mm sapphire window (Powatech GmbH) was placed over the exposed brain surface, immobilized with a customized fixture apparatus, and affixed with a bonding agent (Gluma Comfort Bond; Heraeus Kulzer) and light-curing composite (EvoFlow; Ivoclar). In the end, animals were injected with buprenorphine (0.1 mg/kg; Temgesic; Indivior Schweiz AG; s.c.), carprofen (10 mg/kg; Rimadyl; Zoetis; s.c.), Ringerfundin (10 ml/kg; s.c.) and an antagonist mix of flumazenil (0.5 mg/kg; Anexate; Cheplapharm; s.c.) and atipamezole (2.5 mg/kg; Revertor; Virbac; s.c.) for postoperative care. Mice were allowed to recover for at least 3 weeks before the start of the first imaging session.

Transcortical window implantation

A craniotomy was performed as described earlier. Instead of implanting a cortical window, we implanted a transcortical window.[54] After the craniotomy, part of the somatosensory cortex was carefully aspirated, and the brain tissue was removed using a small suction tip (0.4mm, 634847, Ivoclar Vivadent) until the fibers of the corpus callosum were exposed. Once the area was cleared of blood, a stainless-steel cannula with a round 3 mm in diameter coverslip (D263 coverslip, Warner Instruments) glued to the end was inserted into the brain until it made contact with the underlying tissue. The edges of the cannula were then sealed to the skull with a light-curing composite. Mice were allowed to recover for at least 3 weeks before the start of the first imaging session.

In vivo two-photon imaging

All two-photon experiments were conducted using a custom-built ultra-flexible two-photon laser scanning microscope.[90] The system featured a femtosecond-pulsed laser with an adjustable excitation wavelength range of 680-1300 nm, a pulse width of about 120 fs, and an 80 MHz repetition rate (Chameleon Discovery TPC; Coherent; Spectra Physics). A 25x water-immersion objective (W Plan-Apochromat 25x/1.05 NA; Olympus) or 20x water-immersion objective (W Plan-Apochromat; 1.0; DIC VIS-IR; Zeiss) was utilized. The emission light beam was separated from the excitation light using an 825 SP dichroic and further split by dichroic mirrors (506, 560 and 652 nm) into 4 imaging channels equipped with combinations of short-pass and band-pass filters (CH1: 770 SP + 475/64 BP; CH2: 770 SP + 535/50 BP; CH3: 770 SP + 607/70 BP; CH4: 810 SP + 824 SP + 990 SP). The signal was collected and amplified by photon-multiplier modules (CH1-3: H10770PA-40 SEL, Hamamatsu; CH4: H10770PA-50 SEL, Hamamatsu). Control of PMT gain was achieved through custom LabView software. Image control and data acquisition were controlled by a customized version of ScanImage r3.8.1.[85]

Imaging of cerebral vasculature

The cortical vasculature was visualized by an intravenous injection of 50 μl Texas Red dextran (2.5% in aq. NaCl; 70 kDa; Thermo Fisher Scientific, Cat#D1830), FITC dextran (2.5% in aq. NaCl; 70 kDa; Sigma-Aldrich; Cat#46945) or 20 μl Qtracker655 (Thermo Fisher Scientific, Cat#Q21021MP), depending on the mouse line that was used and their expression of fluorescent proteins. At the beginning of each imaging session, an overview z-stack was acquired for orientation purposes.

Blood flow and vascular diameter measurements

Line scans were performed to measure blood flow velocity or vessel diameter. Red blood cell velocity was assessed through a line scan along the vessel midline (0.64 ms/line, recording length of 72 frames (11.8 s)). Line scan data were processed using a custom-designed image processing toolbox (Cellular and Hemodynamics Processing Suite[86]) and the RADON transform[87] in MATLAB (R2023b; MathWorks). By employing a Gaussian-fitted intensity profile perpendicular to the vessel midline, the vessel's diameter was computed at the full-width half maximum (FWHM).

Induction of EC damage

All *in vivo* imaging sessions were conducted under isoflurane anesthesia, with 4% used for induction and 1.25-2% for maintenance. To visualize the vasculature, Texas Red dextran (2.5% in aq. NaCl; 70 kDa; Thermo Fisher Scientific), FITC dextran (2.5% in aq. NaCl; 70 kDa, Sigma-Aldrich), or Qtracker655 (Thermo Fisher Scientific), depending on the mouse line, was injected via tail vein catheter. Initial overview stacks at 512x512 pixels at a frequency of 0.75 Hz were acquired for orientation. Capillaries were selected for induction of EC damage and baseline blood flow velocity and vessel diameter measurements were obtained in those vessels. Subsequently, the probe Ps2P, based on the Zn complex of tetraarylphthalimidoporphyrin (TAPIP), modified with eight glutamic acid residues in the periphery (Ps2P; 3 mg/ml PBS; 30 μM in blood, assumed blood amount 0.078 ml/g body weight) was injected via the tail vein catheter.[32] EC damage was induced by scanning along a 2-3 μm long line in the center of the capillary lumen (vessel midline), typically positioned midway between two branch points, using a wavelength of 960 nm, 30 mW laser power under the objective, a temporal resolution of 0.64 ms/line, and a pixel dwell time of 1.6 μs, until cessation of blood flow (average induction time of ∼60 s). All capillary occlusions were induced within 30 min from the moment of probe injection. In cases of unsuccessful capillary induction (e.g., vessel regaining flow immediately after induction), the procedure was repeated a maximum of two additional times. To simultaneously damage multiple ECs within the same capillary segment, we selected fast scanning points along the capillary segment and cycled through them during induction.

Quantification of microglia responses

Microglial process accumulation was quantified from the GFP channel using Fiji. Images were binarized using an automated thresholding approach (Triangle method[91]), with threshold levels calculated individually for each frame. Microglial process accumulation was quantified from the binarized images by measuring the mean gray value within a circular region of interest (∼43 μm diameter) centered on the lesion site where accumulation was most prominent. Analysis began at the video onset (∼3.5 min post-induction), with the first six time points averaged to define baseline. Subsequent values were averaged in blocks of ten frames and normalized to baseline.

Pharmacological microglia depletion

Chow containing the CSF1R inhibitor PLX3397 (660 mg/kg; Plexxikon) was provided ad libitum for at least 10 days to deplete microglia in the brain.[92]

Local astrocyte ablation

To locally ablate astrocytes, we used a previously developed protocol.[42,93] We first performed a craniotomy and durotomy in Aldh1l1-EGFP mice and then intracerebrally injected a mixture consisting of human complement (15-30 U/ml, Sigma-Aldrich, #S1764) and a human IgG1 recombinant antibody, AQP4-IgG (clone 7-5-53, 1 μg/μl), reconstructed from a clonotypic plasma blast obtained from the CSF of a patient with neuromyelitis optica (NMO).[81] We employed a drawn glass capillary (Drummond PCR micropipettes, Drummond Scientific) with a tip diameter of 35-45 μm and a custom-built microinjector for the injection. In total, 220 nl were injected in 100 μm intervals between 0 and 300 μm depth.

Optical pericyte ablation

Pericytes were optically ablated following a protocol as previously described.[44] Single pericytes were chosen and subjected to a 20 s laser line scan at 725 nm with power below the objective set at 50 mW. The success of pericyte ablation was determined by the dimmed or absent fluorescent signal from the pericyte. Ablation was considered successful if the pericyte's fluorescent signal did not return within the first 5 min post-ablation. If the pericyte persisted after the initial irradiation, the entire process was repeated, with a maximum of four repetitions.

VEGFR2 and mTOR inhibition

VEGFR2 signaling was inhibited by the i.p. injection of the monoclonal antibody DC101 (anti-mouse VEGFR2; 20 mg/kg in PBS; Bio X Cell, Cat#BE0060) immediately post-induction. As a control, we used the corresponding isotype control antibody (20 mg/kg in PBS; Bio X Cell, Cat#BE0088).

mTOR signaling was inhibited by the i.p. injection of Ku-0063794 (8 mg/kg in 90% corn oil / 10% DMSO (v/v); MedChemExpress, Cat#HY-50710) administered 24 h prior to EC injury induction and again 1 h post-induction. Control animals received vehicle only (90% corn oil / 10% DMSO (v/v)).

Immunohistochemistry

Claudin5-EGFP mice were anesthetized with pentobarbital and transcardially perfused with ice-cold 2% paraformaldehyde (PFA, Paraformaldehyde Granular, Electron Microscopy Sciences, Hatfield, PA) in phosphate-buffered saline (PBS, pH 7.4, (10X Dulbecco's)-Powder, Axon Lab AG, Baden-Dättwil, Switzerland) with a flow of 20 mL/min. Brains were dissected and post-fixed in 4% PFA for 3 h at 4°C. Tissue was cryoprotected in 30% sucrose in PBS for ~2 days at 4°C and then stored at -80°C until cut. 100 μm thick coronal sections were cut using a vibratome (Leica VT1000S). The buffer tray was filled with ice-cold PBS and surrounded by crushed ice. The frozen brain was superglued to the platform and immersed in ice-cold PBS. Once defrosted, the brain was cut with a knife feed speed of approx. 1.0 mm/s (scale setting 8.3) and a frequency of 80 Hz (scale setting 8) and then stored in antifreeze solution (50 mM sodium phosphate buffer pH 7.4, 1 M glucose, 35% ethylene glycol and 3.5 mM sodium azide) at -20°C until further processing. Free-floating sections were washed with 0.05% Triton X-100 (Sigma-Aldrich, Buchs, Switzerland) in Tris buffer (50 mM, pH 7.4). Sections were then incubated with primary antibodies diluted in 0.3% Triton X-100 in Tris buffer containing 5% of normal donkey serum for two nights at 4°C. Primary antibodies used: goat anti-CD13 (1:400, R and D Systems, Cat#AF2335) and rabbit anti-Collagen IV (1:800, Bio-Rad, Cat#2150-1470). After three 30-min washes in 0.05% Triton-X-100 buffer in Tris Buffer, the sections were incubated in secondary antibody solution (0.05% Triton-X-100 in Tris Buffer containing 2% normal donkey serum) overnight at 4°C. Secondary antibodies used: Cy3 anti-goat (1:700, Jackson ImmunoResearch, Labs Cat#705-165-003) and AF647 anti-rabbit (1:700, Thermo Fisher Scientific, Cat#A32795). For nuclei labeling, DAPI (1:10000, Abcam, AB228549) was added to the secondary antibody solution. Sections were mounted on SuperFrost Plus slides (Thermo Scientific) and covered with Dako Fluorescence Mounting Medium (Dako, Jena, Germany).

Confocal image acquisition and analysis

Tiled z-stacked (z-stack step size: 1 μm) confocal images were acquired using a Zeiss LSM 800 confocal laser scanning microscope and the 40x objective (Plan-Apochromat, NA 1.4, Oil DIC (UV) VIS-IR). Tiled images (cortex: 2 x 4 tiles, hippocampus: 3 x 2 tiles) were automatically aligned with the built-in microscope software (ZEN blue software, Zeiss). Confocal images shown represent 3D volumes of the cortex and hippocampus. Image analysis was performed with Imaris (Imaris x 64, Oxford Instruments, Version 10.2.0). First, a surface layer was added, and the vessels were segmented using Imaris' machine learning option using the EGFP channel (Claudin5-EGFP) and the collagen IV channel. The surface layer was then utilized to create a binarized channel, which was subsequently used to calculate the filaments with the filament layer (skeleton of the vessels). The filaments were manually proofread and corrected. The number of ECs (cell bodies) per filament was counted manually. Cell nuclei were identified using Claudin5-EGFP and DAPI staining, while CD13 staining, specific for pericytes, was employed to exclude the misidentification of pericytes as ECs.

Please cite this article in press as: Condrau et al., Intrinsic endothelial remodeling drives brain capillary repair, Neuron (2026), https://doi.org/10.1016/j.neuron.2026.04.020

For statistics, Imaris detailed specific values for segment volume, segment length, segment mean diameter, and segment straightness were extracted. For density calculations (length density, volume fraction, segment density, branch point density), all vessel segments in the picture were used. Capillaries were defined as vessels with an abluminal diameter (includes endothelial cells and basement membrane) of $\leq$5.2 μm, which amounted to 50% of the total number of vascular segments in the data set. Capillary segments comprise the vast majority of total vessel segments (typically 60-80%),[51,94] hence the chosen threshold (50%) ensures that no precapillary arterioles were included in the statistics. For quantification of EC numbers per capillary segment and for comparison of individual segment length and straightness, terminal segments were excluded, to ensure that only fully captured capillaries (i.e., not truncated by the sectioning plane) were analyzed. Only a random subset of the acquired data was used for manual quantification of ECs per capillary segment, while the whole dataset was used for the density calculations.

For the analysis, one image from each four brain sections from each three animals was analyzed for the cortex and hippocampus. Pictures were taken in the somatosensory cortex and in the stratum radiatum of the hippocampus using the DAPI channel for region of interest selection.

Two-photon image analysis

All two-photon images were processed using FIJI (ImageJ 2.1.0). The individual channels were merged, and maximum intensity two-photon projections were generated, as specified in the figure legend. In non-quantitative images, the gamma value was non-linearly adjusted to enhance the visibility of low-intensity objects.

Graphical illustrations were created using Affinity Designer (Serif Europe, UK) and Biorender (Biorender, Toronto, CA). Vascular leakage was assessed qualitatively by determining whether Ps2P (~3 kDa) extravasation into the surrounding tissue was detectable.

QUANTIFICATION AND STATISTICAL ANALYSIS

Histological data quantification and analysis

Histological statistical analyses were performed using R (version 4.4.2). The lme4 package for linear and generalized mixed effects models (lmer and glmer function of lme4: R package version 1.1-35.4[95]) was used to examine the effect of brain region (= fixed effect) on the variable of interest. A linear mixed effect model, which included a random intercept for each animal and image as covariate, was applied to normally distributed data. Values for differences between brain regions were obtained post-hoc using the *means* package with pairwise comparisons (R package version 1.10.5.1[96]) and the Kenward-Roger method to calculate degrees of freedom. Non-normally distributed data were modeled using a generalized linear mixed model (GLMM) with Gamma distribution where possible. The model included a random intercept for each animal and image nested within animal. Values for differences between brain regions were obtained using the *lmerTest* package (R package version 3.1-3) using Satterthwaite approximation for degrees of freedom. Alternatively, non-normally distributed data were compared using an unpaired Wilcoxon rank-sum test (Mann-Whitney U Test) using the *wilcox.test()* function from the *stats* package (R package version 4.4.2). To compare the relationship between vessel segment length and the number of ECs per segment in the two brain regions, we used a Spearman rank correlation test for non-parametric data. Fisher's Z-transformation was used to transform the Spearman correlation coefficients into a normal distribution, followed by a Fisher's Z-test. All data are presented as mean ± SEM. p-values $\leq$ 0.05 were considered statistically significant and are stated together with the sample size and the test used in the figure legends.

Two-photon data quantification and analysis

Quantitative datasets were processed in Excel (Microsoft Corporation; Redmond; WA; USA), and GraphPad Prism (version 10.0; GraphPad Software; La Jolla; CA; USA) was used for statistical analysis. The respective statistical tests and group size (N = number of animals, n = number of capillaries) are indicated in figure legends.

Results are presented as mean ± SEM (standard error of the mean). D'Agostino-Pearson omnibus normality test was applied to assess normality within a dataset. For normally distributed data, unpaired Student's t-test or paired t-test was utilized to determine significance between two groups. In cases of non-normally distributed data, the Mann-Whitney test was employed. A comparison of three groups was statistically analyzed using an ANOVA or the Kruskal-Wallis (unpaired data) or Friedman (paired data) test and Dunn's test for multiple comparisons. To account for vessels nested within mice, linear mixed models were applied where appropriate.